Theoretical investigation of the pDRM process: a flexible lock-in function approach

Lukas Bohsung[1], Maximilian Arthus Schanner[2], Monika Korte[2], and Matthias Holschneider[3]

[1]GFZ German Research Centre for Geosciences
[2]GFZ German Research Center for Geosciences
[3]University of Potsdam

July 20, 2023

Abstract

The primary data sources for reconstructing the geomagnetic field of the past millennia are archaeomagnetic and sedimentary paleomagnetic data. Sediment records, in particular, are crucial in extending the temporal and spatial coverage of global geomagnetic field models, especially when archaeomagnetic data is sparse. However, the post-depositional detrital remanent magnetization (pDRM) process is still poorly understood and can cause smoothing of the magnetic signal and offsets with respect to the sediment age. To make effective use of sedimentary data, it is essential to understand the lock-in process and its impact on the magnetic signal. In this study, we investigate the lock-in process theoretically and derive a parameterized lock-in function that can approximate possible lock-in behaviors. Additionally, we demonstrate that a lock-in function that is independent of absolute parameters can only be applied to the magnetic direction components (declination and inclination), but not to the relative intensity. Integrating this lock-in function into the ArchKalmag14k modeling procedure (missing citation) allows including data from sediment records. The parameters of the lock-in function are estimated by the maximum likelihood method using archaeomagnetic data as a reference. The effectiveness of the proposed method is evaluated through synthetic tests. Additionally, we apply our technique to sediment records from two lakes in Sweden (Kälksjön and Gyltigesjön) as first case studies. Our results demonstrate that the proposed method is capable of effectively correcting the distortion caused by the lock-in process, making data from sedimentary records a more reliable and informative source for geomagnetic field reconstructions.

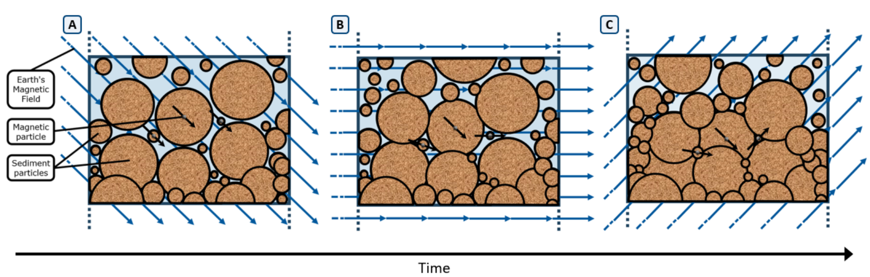

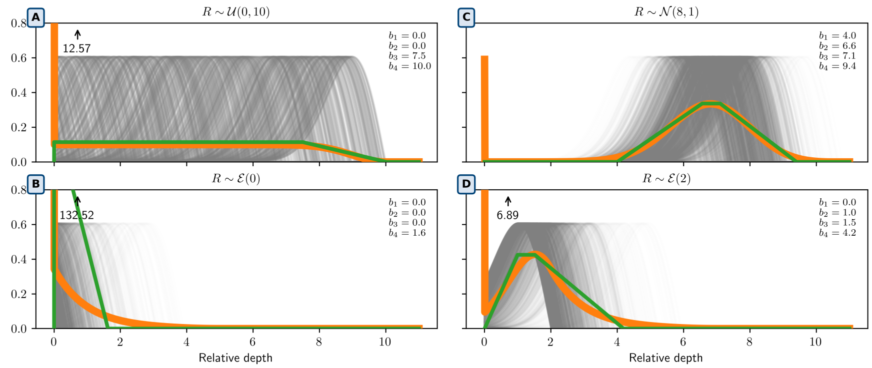
A
$R \sim \mathcal{U}(0,10)$
12.57
$b_1 = 0.0$ $b_2 = 0.0$ $b_3 = 7.5$ $b_4 = 10.0$
B
$R \sim \mathcal{E}(0)$
132.52
$b_1 = 0.0$ $b_2 = 0.0$ $b_3 = 0.0$ $b_4 = 1.6$
C
$R \sim \mathcal{N}(8,1)$
$b_1 = 4.0$ $b_2 = 6.6$ $b_3 = 7.1$ $b_4 = 9.4$
D
$R \sim \mathcal{E}(2)$
6.89
$b_1 = 0.0$ $b_2 = 1.0$ $b_3 = 1.5$ $b_4 = 4.2$
Relative depth
Relative depth

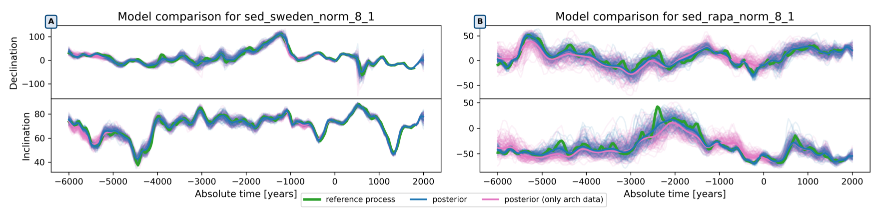
A
Model comparison for sed_sweden_norm_8_1
B
Model comparison for sed_rapa_norm_8_1
Declination
Inclination
Absolute time [years]
Absolute time [years]
reference process
posterior
posterior (only arch data)

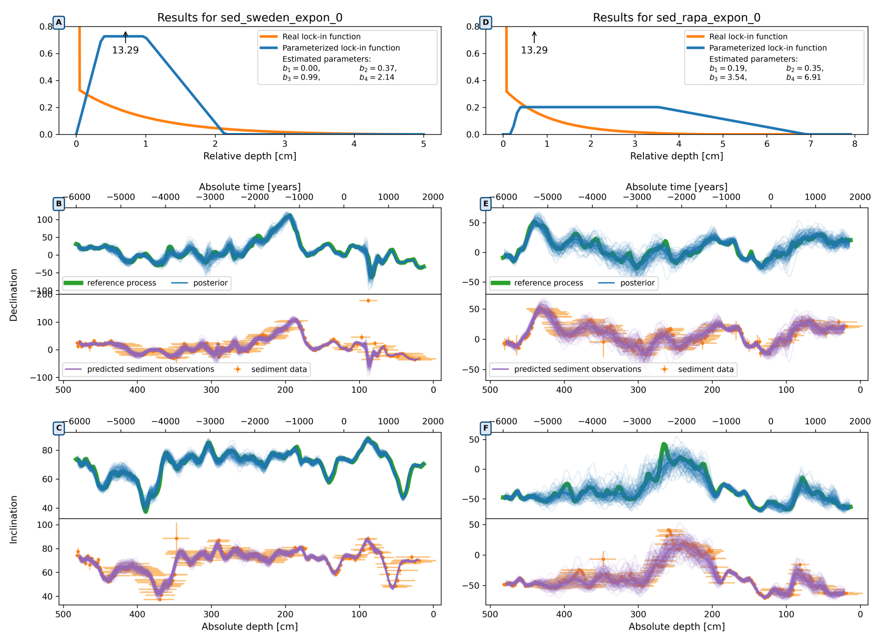
A
Results for sed_sweden_expon_0
Real lock-in function
Parameterized lock-in function
Estimated parameters:
$b_1 = 0.00$, $b_2 = 0.37$, $b_3 = 0.99$, $b_4 = 2.14$
13.29
Relative depth [cm]
D
Results for sed_rapa_expon_0
Real lock-in function
Parameterized lock-in function
Estimated parameters:
$b_1 = 0.19$, $b_2 = 0.35$, $b_3 = 3.54$, $b_4 = 6.91$
13.29
Relative depth [cm]
B
E
C
F
Absolute time [years]
Declination
Inclination
reference process
posterior
predicted sediment observations
sediment data
Absolute depth [cm]
Absolute depth [cm]

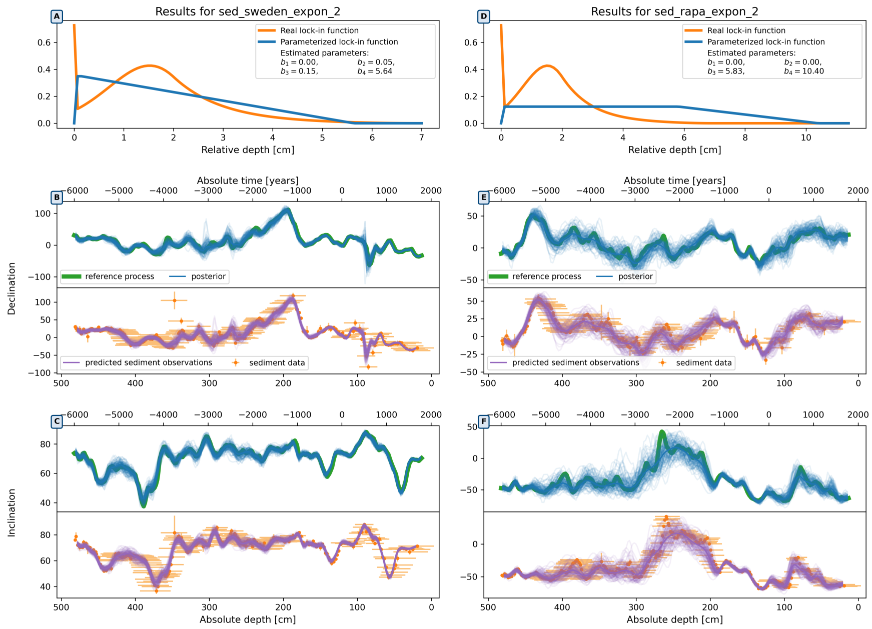
Results for sed_sweden_expon_2
Results for sed_rapa_expon_2
Real lock-in function
Parameterized lock-in function
Estimated parameters:
$b_1 = 0.00$, $b_2 = 0.05$, $b_3 = 0.15$, $b_4 = 5.64$
$b_1 = 0.00$, $b_2 = 0.00$, $b_3 = 5.83$, $b_4 = 10.40$
Relative depth [cm]
Absolute time [years]
Declination
Inclination
reference process
posterior
predicted sediment observations
sediment data
Absolute depth [cm]

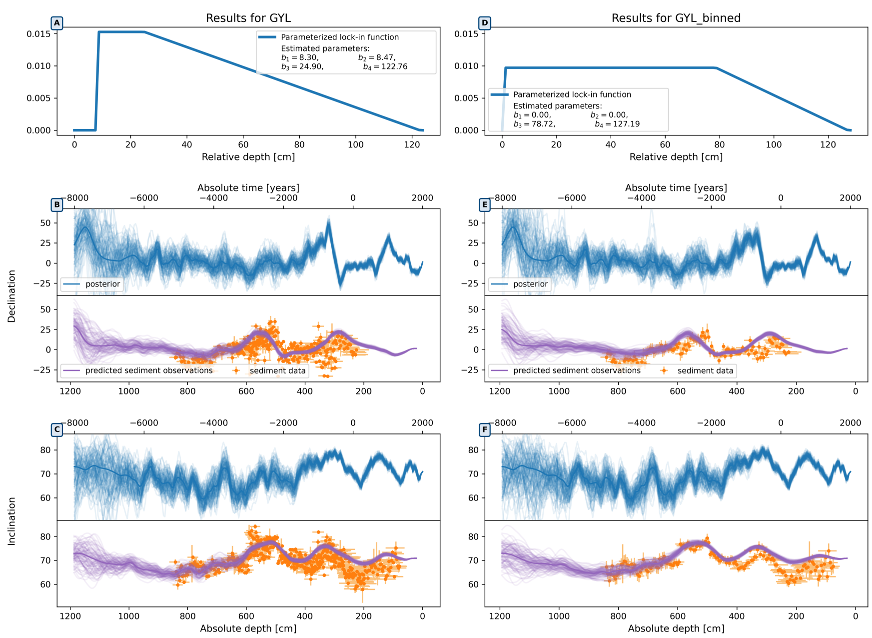
Results for GYL
Results for GYL_binned
Parameterized lock-in function
Estimated parameters:
$b_1 = 8.30$, $b_2 = 8.47$, $b_3 = 24.90$, $b_4 = 122.76$
$b_1 = 0.00$, $b_2 = 0.00$, $b_3 = 78.72$, $b_4 = 127.19$
Relative depth [cm]
Absolute time [years]
Declination
Inclination
posterior
predicted sediment observations
sediment data
Absolute depth [cm]

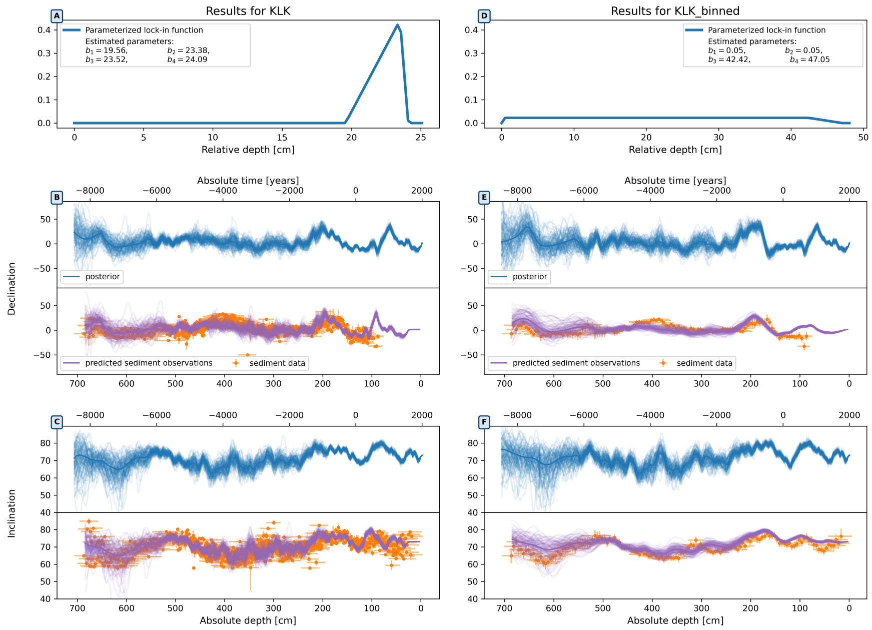
Results for KLK
Parameterized lock-in function
Estimated parameters:
$b_1 = 19.56$, $b_2 = 23.38$,
$b_3 = 23.52$, $b_4 = 24.09$
Relative depth [cm]
Results for KLK_binned
Parameterized lock-in function
Estimated parameters:
$b_1 = 0.05$, $b_2 = 0.05$,
$b_3 = 42.42$, $b_4 = 47.05$
Relative depth [cm]
Absolute time [years]
Declination
posterior
predicted sediment observations
sediment data
Inclination
Absolute depth [cm]

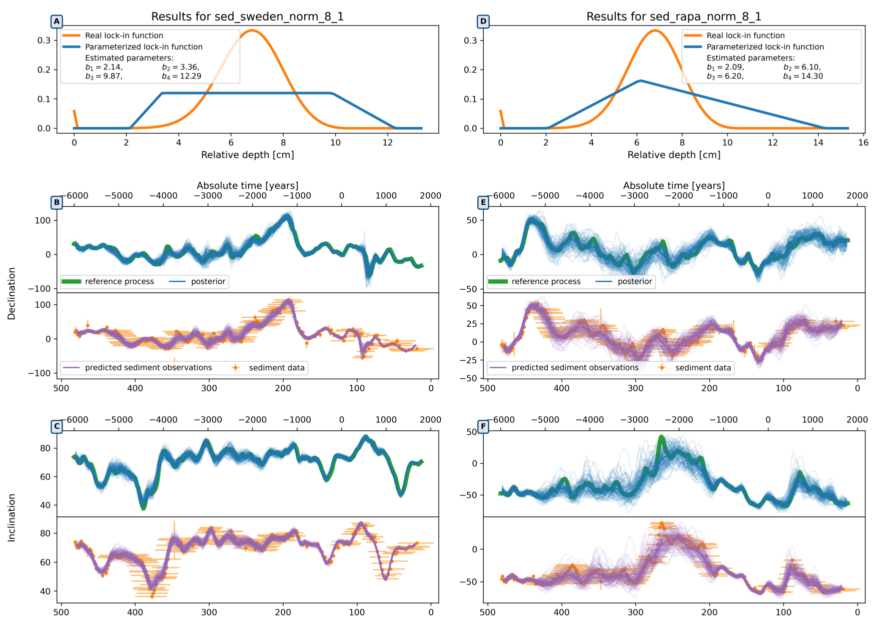
Results for sed_sweden_norm_8_1
Real lock-in function
Parameterized lock-in function
Estimated parameters:
$b_1 = 2.14$, $b_2 = 3.36$,
$b_3 = 9.87$, $b_4 = 12.29$
Relative depth [cm]
Results for sed_rapa_norm_8_1
Real lock-in function
Parameterized lock-in function
Estimated parameters:
$b_1 = 2.09$, $b_2 = 6.10$,
$b_3 = 6.20$, $b_4 = 14.30$
Relative depth [cm]
Absolute time [years]
Declination
reference process
posterior
predicted sediment observations
sediment data
Inclination
Absolute depth [cm]

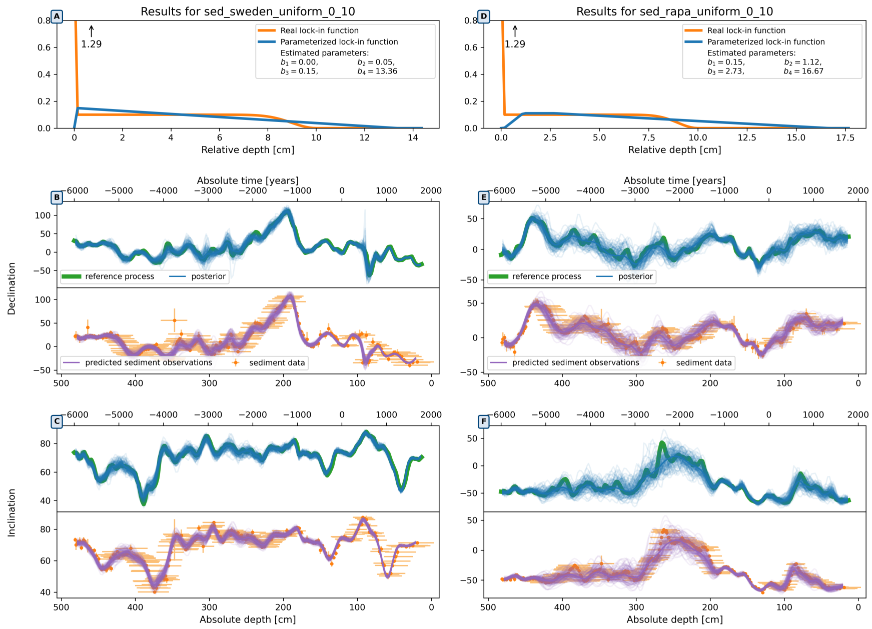

Results for sed_sweden_uniform_0_10
Results for sed_rapa_uniform_0_10
A
D
1.29
Real lock-in function
Parameterized lock-in function
Estimated parameters:
$b_1 = 0.00$, $b_2 = 0.05$, $b_3 = 0.15$, $b_4 = 13.36$
$b_1 = 0.15$, $b_2 = 1.12$, $b_3 = 2.73$, $b_4 = 16.67$
Relative depth [cm]
Absolute time [years]
B
E
C
F
Declination
Inclination
reference process
posterior
predicted sediment observations
sediment data
Absolute depth [cm]

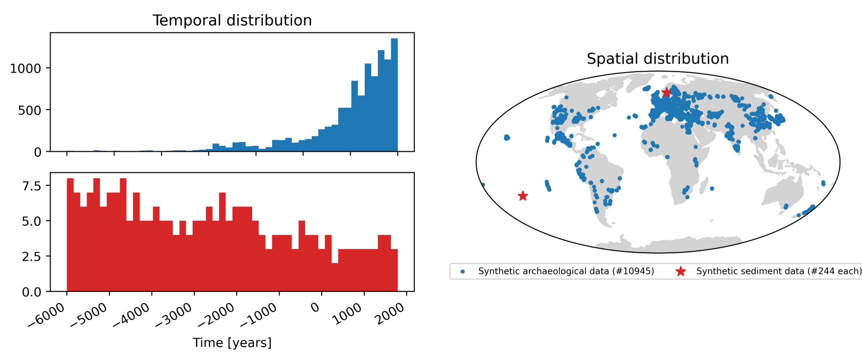

Temporal distribution
Time [years]
Spatial distribution
Synthetic archaeological data (#10945)
Synthetic sediment data (#244 each)

References

Theoretical investigation of the pDRM process: a flexible lock-in function approach

L. Bohsung[1,2], M. Schanner[1,2], M. Korte[1], M. Holschneider[2]

[1]GFZ German Research Centre for Geosciences, Section 2.3, Potsdam, Germany
[2]University of Potsdam, Applied Mathematics, Potsdam, Germany

Key Points:

- We present a theoretical investigation of the pDRM process.
- A new class of lock-in functions is presented capable of approximating all possible lock-in behaviors.
- The proposed method is evaluated through several synthetic tests.

Corresponding author: Lukas Bohsung, `lbohsung@gfz-potsdam.de`

Abstract

The primary data sources for reconstructing the geomagnetic field of the past millennia are archaeomagnetic and sedimentary paleomagnetic data. Sediment records, in particular, are crucial in extending the temporal and spatial coverage of global geomagnetic field models, especially when archaeomagnetic data is sparse. However, the post-depositional detrital remanent magnetization (pDRM) process is still poorly understood and can cause smoothing of the magnetic signal and offsets with respect to the sediment age. To make effective use of sedimentary data, it is essential to understand the lock-in process and its impact on the magnetic signal. In this study, we investigate the lock-in process theoretically and derive a parameterized lock-in function that can approximate possible lock-in behaviors. Additionally, we demonstrate that a lock-in function that is independent of absolute parameters can only be applied to the magnetic direction components (declination and inclination), but not to the relative intensity. Integrating this lock-in function into the ArchKalmag14k modeling procedure (Schanner et al., 2022) allows including data from sediment records. The parameters of the lock-in function are estimated by the maximum likelihood method using archaeomagnetic data as a reference. The effectiveness of the proposed method is evaluated through synthetic tests. Additionally, we apply our technique to sediment records from two lakes in Sweden (Kälksjön and Gyltigesjön) as first case studies. Our results demonstrate that the proposed method is capable of effectively correcting the distortion caused by the lock-in process, making data from sedimentary records a more reliable and informative source for geomagnetic field reconstructions.

Plain Language Summary

Our paper discusses how to use sedimentary data to reconstruct the geomagnetic field in the past. When we study the geomagnetic field of the past, we rely on data from archaeological and sedimentary sources. However, there is a problem with sediment records called post-depositional detrital remanent magnetization (pDRM), which can make the magnetic signal unclear and cause sediment age to be offset.

To make the sedimentary data more reliable, we developed a new method to correct the distortion caused by pDRM. Our method involves creating a mathematical model of the lock-in process, which helps to explain the behavior of magnetic particles in sediments over time. We then use this model and archaeological records to estimate parameters of the lock-in process.

Once we have determined the parameters of the lock-in process, we can use them to correct the distortion caused by pDRM in sedimentary data. We tested our method on synthetic data and two sediment records from lakes in Sweden, and our results show that it is effective in correcting the distortion caused by pDRM and making sedimentary data more reliable for reconstructing the geomagnetic field.

1 Introduction

Over the last decades many data-based models of the geomagnetic field have been developed (e.g. Arneitz et al., 2019; Constable et al., 2016; Hellio & Gillet, 2018; Nilsson & Suttie, 2021; Schanner et al., 2022). Based on different data collections and modeling methods, each model covers different areas and time periods with varying degrees of accuracy and uncertainty. One important data set for models of the geomagnetic field of the past millennia is provided by archaeomagnetic data. Archaeomagnetic data can deliver valuable and useful information about the geomagnetic field. However, the highly uneven data coverage, both in space and time poses a great challenge. An additional data source that covers larger time periods and improves the spatial coverage is provided by sedimentary records.

The magnetization process in sediments differs from the magnetization of archaeological materials. In archaeological materials, as well as in lava flows, the fairly well understood thermoremanent magnetization (TRM) occurs when the material cools down from above the maximum Curie temperature (e.g. Stacey, 2012). When the temperature is above the maximum Curie temperature, the magnetic particles in the material lose their magnetic properties. When they cool down the magnetic moments align with the geomagnetic field, and further cooling causes them to be locked in.

While the lock-in process in the TRM occurs on short time scales (hours to weeks), the lock-in time of magnetic moments in sediment records can be much longer (years to centuries). The magnetization in sediments is called detrital remanent magnetization (DRM), which was first measured by McNish and Johnson (1938). During the sedimentation process, magnetic particles are deposited in such a way that their magnetic moments tend to point in the direction of the geomagnetic field while interaction with other particles and the ongoing solidification increasingly impede the particles to fully align. Additional sediment particles lead to a consolidation of the underlying layers and thus to a mechanical lock-in of the magnetic particles. The magnetization in sediments is affected by the interaction of the magnetic particles with the substrate at the sediment water interface and by dewatering of the sediment (Irving, 1957). The terminology and classification of these effects are not completely consistent in the literature. In the following we will be using the terminology recommended in the review by Verosub (1977). According to Verosub (1977) the term DRM refers to the remanent magnetization found in sediments. By depositional DRM (dDRM) we describe the magnetization acquired by the interaction of the particles with the substrate at the sediment/water interface. The term post-depositional DRM (pDRM) refers to the longer timescale and describes any magnetization that is acquired after the particle settled on the sediment/water interface.

There are various effects that are summarized in the term dDRM. One example is the inclination error, which occurs when non-spherical particles settle flat on the sediment/water interface. This leads to a distortion of the inclination to smaller values (King, 1955). Another distortion of the inclination can occur when aligned particles roll into the nearest depression of the sediment/water interface (Griffiths et al., 1960).

In this paper, we will focus on the investigation of the post-depositional DRM. In general, only coarse-grained fractions are mechanically fixed more or less immediately after deposition. Smaller particles which are embedded in water-filled voids or pore spaces of the sediment can move freely for a longer period of time (Irving, 1957). With progressive consolidation and dewatering of the sediment, also these particles become locked in. Figure 1 illustrates the complete lock-in process. (**A**) The lock-in process begins when

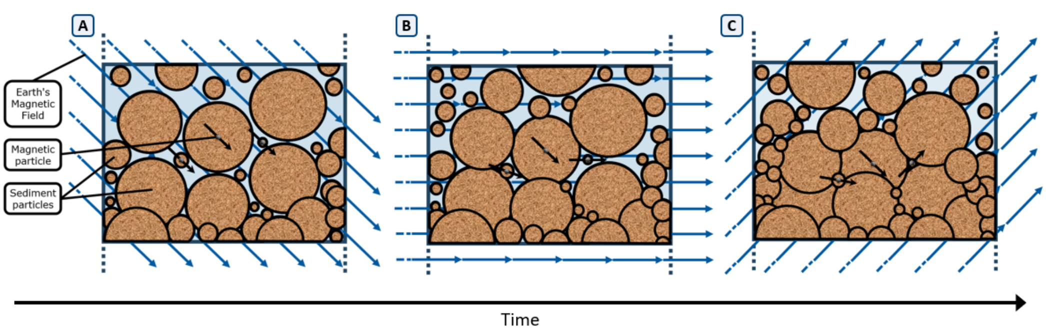

Figure 1. Visualization of the lock-in process by three time steps (**A**) to (**C**). The blue arrows indicate the geomagnetic field direction, with a strong change from (**A**) to (**C**) for illustration purposes. The magnetization direction of magnetic sediment particles is indicated by black arrows.

the particles passed the mixed surface layer and reach the lock-in area. Typically, sediments consist of both magnetic and non-magnetic particles. During the initial stages of the lock-in process, all particles are completely free to move. Therefore, the magnetic particles align themselves with the geomagnetic field (blue arrows). For visualization reasons, we have exaggerated the alterations in the geomagnetic field direction during the lock-in process. (**B**) The surrounding material becomes consolidated by the sedimentation process, and larger magnetic particles gradually lose their mobility and become locked-in, whereas smaller carriers remain mobile and continue to follow the changes in the geomagnetic field. (**C**) After sufficient sedimentation and consolidation, the lock-in process reaches completion, with each particle bearing information regarding diverse states of the geomagnetic field throughout the lock-in period. Thus, the magnetic moment of the entire layer becomes a weighted sum of the geomagnetic field over the lock-in time.

The different lock-in times of magnetic particles in a layer lead to a delayed and smoothed signal of the geomagnetic field in the record. In other words, the magnetic moment of a layer is a weighted average of the geomagnetic field signal over the lock-in time of all particles contained in the layer. The weights are given by lock-in functions.

Over the last decades many lock-in functions have been suggested. Exponential lock-in functions (e.g. Løvlie, 1976; Kent & Schneider, 1995), constant (e.g. Bleil & Von Dobeneck, 1999), linear (e.g. Meynadier & Valet, 1996), cubic (e.g. Roberts & Winklhofer, 2004), Gaussian (e.g. Suganuma et al., 2011) and parameterized lock-in functions that can cover multiple classes (e.g. Nilsson et al., 2018).

Inspired by the large variety of possible lock-in functions, we present a theoretical investigation of the lock-in process and the derivation of a general parameterized lock-in function capable of approximating any possible lock-in function. Additionally, we demonstrate that a lock-in function that is independent of absolute parameters can only be applied to the magnetic direction components (declination and inclination), but not to the relative intensity.

An advancement of the ArchKalmag14k modeling procedure (Schanner et al., 2022) allows including data from sediment records. To estimate the parameters of the lock-in function we use maximum likelihood methods where archaeomagnetic data serve as reference.

In section 2 we first briefly outline the geomagnetic field modeling method and then develop the pDRM modeling. We test the new method first with synthetic data and then apply it to two real data examples in section 3. We discuss some findings and give an outlook to future work in section 4 before ending with summarizing conclusions.

2 Modeling Concept

2.1 Geomagnetic Field Model

We will model the geomagnetic field by using a Bayesian approach based on Gaussian Processes. Every Gaussian Process is uniquely defined by a mean and a covariance function (Rasmussen, 2004).

As in Schanner et al. (2022) we use a Bayesian approach and describe the geomagnetic field as the realization of a Gaussian Process

$$\mathbf{B} \sim \mathcal{GP}(\bar{\mathbf{B}}, K_{\mathbf{B}}) \tag{1}$$

with constant (space, time) mean function $\bar{\mathbf{B}}\colon \mathbb{S}^2 \times \mathbb{R} \to \mathbb{R}^3$ and kernel function $K_{\mathbf{B}}\colon (\mathbb{S}^2 \times \mathbb{R})^2 \to \mathbb{R}^{3\times 3}$, where $\mathbb{S}^2 = \{x \in \mathbb{R}^3 \mid \|x\| = 1\}$ denotes the standard 2-sphere associated to the space variable. Therefore, the the knowledge about the geomagnetic field and its uncertainty is a distribution of functions $\mathbf{B}\colon \mathbb{S}^2 \times \mathbb{R} \to \mathbb{R}^3$. In the following we will model the lock-in process for a single sediment core sample and treat the space variable as a constant, i.e. we will consider $\mathbf{B}$ as a Gaussian process of time only.

We follow the a priori assumptions of Schanner et al. (2022) and use the estimated hyperparameters given in Table 2 of Schanner et al. (2022). Hence, we assume that all

Gauss coefficients are a priori uncorrelated at a reference radius $R = 2800\,\mathrm{km}$ with zero mean except for the axial dipole. For the axial dipole we assume a constant mean value of $\gamma_1^0 = -38\,\mu\mathrm{T}$ (at the Earth's surface). Further, we assume an a priori variance $\alpha_{DP} = 39\,\mu\mathrm{T}$ for the dipole and an a priori variance $\alpha_{ND} = 118.22\,\mu\mathrm{T}$ for all higher degrees (at the reference radius). The temporal correlation of the Gauss coefficients is given by

$$\rho_l(\Delta t) = \left(1 + \frac{|\Delta t|}{\tau_l}\right) \mathrm{e}^{-\frac{|\Delta t|}{\tau_l}}$$

where the correlation time is given by $\tau_l = \begin{cases} 171.34\,\mathrm{yrs} & l = 1 \text{ (dipole)} \\ \frac{379.59}{l}\,\mathrm{yrs} & l > 1 \text{ (non-dipole)} \end{cases}$.

2.2 Lock-in Process

The key part of this section is the modeling of the pDRM described in the introduction. For this purpose we will start by investigating the rotational dynamics of a single particle during the lock-in process. Subsequently, we will expand the results to a whole layer and derive a general parameterized lock-in function.

Let $\mathbf{M}_p \colon \mathbb{R} \to \mathbb{R}^3$ be the time varying magnetic moment of a particle p. During the sedimentation process, the behavior of a particle strongly depends on its size, shape and the magnitude of its magnetization. We assume that each particle has a constant magnitude of magnetization, i.e. for all $t \in \mathbb{R}$ we assume $\|\mathbf{M}_p(t)\| = \mathrm{M}_p \in \mathbb{R}$. This assumption leads to the first differential equation

$$\dot{\mathbf{M}}_p = \boldsymbol{\omega}_p \times \mathbf{M}_p \tag{2}$$

where $\boldsymbol{\omega}_p \colon \mathbb{R} \to \mathbb{R}^3$ is the angular velocity of particle p and $\times$ denotes the cross product.

Let $\mathbf{I}_p \in \mathbb{R}^{3\times 3}$ be the moment of inertia of particle p. We assume that there are two torques influencing the rotational dynamics of the particle. They are due to the geomagnetic field, denoted by $\mathbf{M}_p \times \mathbf{B}$, and the surrounding material. For the latter we assume a simple heuristic viscous frictional law of the form $-\frac{1}{\gamma}\boldsymbol{\omega}_p$, where γ is a function corresponding to the torque generated by the surrounding material which can come from a variety of sources such as friction, gravity, or other electromagnetic forces. Newton's second law of rotational motion states that the net torque acting on a particle is equal to the product of its moment of inertia and angular acceleration, i.e.

$$\mathbf{I}_p \dot{\boldsymbol{\omega}}_p = \mathbf{M}_p \times \mathbf{B} - \frac{1}{\gamma}\boldsymbol{\omega}_p \tag{3}$$

The larger the function value of γ, the less influence on the rotational dynamics comes from the surrounding material. In other words, a larger function value of γ corresponds to higher mobility of the particle. In the following the function γ is called the mobility function of the particle.

Since the particle is turning very slowly, the total angular momentum on the left side of equation (3) may be neglected, and we obtain the following relation

$$\boldsymbol{\omega}_p = \gamma \mathbf{M}_p \times \mathbf{B}$$

Using this solution we can reformulate equation (2) as

$$\dot{\mathbf{M}}_p = -\gamma \mathbf{M}_p \times (\mathbf{M}_p \times \mathbf{B})$$

Since the magnitude of the particle's magnetization is assumed to be constant, we can write the magnetic moment as $\mathbf{M}_p(t) = \mathrm{M}\mathbf{e}_{\mathbf{M}_p}(t)$ where $\mathbf{e}_{\mathbf{M}_p} \colon \mathbb{R} \to \mathbb{S}^2$ is a unit vector in the direction of the particle's magnetization. Similarly, but with non-constant magnitude $\mathrm{B} \colon \mathbb{R} \to \mathbb{R}$, the geomagnetic field can be written as $\mathbf{B}(t) = \mathrm{B}(t)\mathbf{e}_{\mathbf{B}}(t)$ where

$\mathbf{e_B} : \mathbb{R} \to \mathbb{S}^2$ is a unit vector in the direction of the geomagnetic field. This leads to

$$\begin{aligned} \dot{\mathbf{e}}_{\mathbf{M}_p} &= -\gamma \mathbf{e}_{\mathbf{M}_p} \times \big(\mathrm{M}\mathbf{e}_{\mathbf{M}_p} \times \mathrm{B}\mathbf{e}_{\mathbf{B}}\big) \\ &= -\gamma \mathrm{MB}\mathbf{e}_{\mathbf{M}_p} \times \big(\mathbf{e}_{\mathbf{M}_p} \times \mathbf{e}_{\mathbf{B}}\big) \\ &= -\gamma^{\mathrm{B}(t)}_{\tau_p, r_{\tau_p}} \mathbf{e}_{\mathbf{M}_p} \times \big(\mathbf{e}_{\mathbf{M}_p} \times \mathbf{e}_{\mathbf{B}}\big) \end{aligned}$$

where $\tau_p \in \mathbb{R}$ denotes the time when the particle begins to lock in and $\tau_p + r_{\tau_p} \in \mathbb{R}$ the time when the particle is completely locked in. Note that the lock-in duration, r_{τ_p}, depends on the sedimentation rate. The new mobility function $\gamma^{\mathrm{B}(t)}_{\tau_p, r_{\tau_p}}$ will be described in the next paragraph.

We assume that the particle aligns with the geomagnetic field before the lock-in process begins. Formally, we have to set γ to infinity for all $t \leq \tau_p$. As soon as the lock-in process begins, γ becomes finite and decreases monotonically to zero. During the lock-in process the mobility of the particle depends on the magnitude M of its magnetization and the intensity of the geomagnetic field $\mathrm{B}(t)$. With completion of the lock-in process, the particle becomes immobile, and the mobility function becomes constant zero. Therefore, we shall consider effective mobility functions of the following form $\gamma^{\mathrm{B}(t)}_{\tau_p, r_{\tau_p}} : \mathbb{R} \to \mathbb{R}$ with

$$\gamma^{\mathrm{B}(t)}_{\tau_p, r_{\tau_p}}(t) = \begin{cases} \infty & t \leq \tau_p \\ \mathrm{MB}(t)\gamma(t) & t \in (\tau_p, \tau_p + r_{\tau_p}) \\ 0 & t \geq \tau_p + r_{\tau_p} \end{cases}$$

where γ is a monotonically decreasing function with $\lim_{t \to r_{\tau_p}} \gamma(\tau_p + t) = 0$.

We want to derive a lock-in function that can be applied to each layer of the sediment core sample, as it is done in Nilsson et al. (2018). In other words, the lock-in function of a whole layer has to be independent of absolute values, such as the absolute time or depth when the lock-in process began. The lock-in function of a whole layer will depend on the individual lock-in functions of the particles contained in the layer. These individual lock-in functions will depend on the individual mobility functions. Obviously, the derived mobility function is influenced by two parameters that depend on the absolute time, through the lock-in duration r_{τ_p} on the one hand, and the intensity of the geomagnetic field on the other.

The first dependency is influenced by the sedimentation rate. By defining the lock-in function in depth rather than time we overcome this dependency. The only assumption we have to make here is that the sedimentation material does not change considerably. We will first derive the lock-in function in time and convert it to depth afterwards.

The geomagnetic field's intensity function must be approximated by a constant value in order to overcome the second dependency. This approach will lead to a lock-in function that is independent of absolute depth and can therefore be applied to each layer of the sediment core sample. However, this assumption prevents us from simulating the intensity of the geomagnetic field. This is a generic issue for all lock-in functions that are independent of absolute parameters. Nevertheless, even with this strong approximation, we can still derive a lock-in function that provides a useful model for the directional components.

We approximate the geomagnetic field intensity by its mean over the absolute time of the sediment core sample and denote it by $\bar{\mathrm{B}}$. Additionally, we set the time when the particles' mobility function becomes finite to the time when the first particle in the layer begins to lock-in. We denote this time by τ. Furthermore, we set $r_{p,\tau} = \tau_p + r_{\tau_p} - \tau$. Then the mobility function is given by

$$\gamma_{\tau, r_{p,\tau}}(t) = \begin{cases} \infty & t \leq \tau \\ \mathrm{M}\bar{\mathrm{B}}\gamma(t) & t \in (\tau, \tau + r_{p,\tau}) \\ 0 & t \geq \tau + r_{p,\tau} \end{cases}$$

The directions of the particles' magnetic moment during the lock-in process can then be described by the solution of the following differential equation with initial condition

$$\begin{aligned} \dot{\mathbf{e}}_{\mathbf{M}_p} &= -\gamma_{\tau,r_{p,\tau}} \mathbf{e}_{\mathbf{M}_p} \times \left(\mathbf{e}_{\mathbf{M}_p} \times \mathbf{e}_{\mathbf{B}}\right) \\ \mathbf{e}_{\mathbf{M}_p}(\tau) &= \mathbf{e}_{\mathbf{B}}(\tau) \end{aligned} \tag{4}$$

For all $t \geq \tau$ the differential equation in (4) can be approximated by a first order linear ordinary differential equation of the form

$$\begin{aligned} \dot{\mathbf{m}}_p &= -\gamma_{\tau,r_{p,\tau}} (\mathbf{m}_p - \mathbf{b}) \\ \mathbf{m}_p(\tau) &= \mathbf{b}(\tau) \end{aligned} \tag{5}$$

where $\mathbf{m}_p \colon [\tau, \infty) \to \mathbb{R}^2$ and $\mathbf{b} \colon [\tau, \infty) \to \mathbb{R}^2$.

The idea of this approximation is to project the three-dimensional unit vectors onto the tangent plane of the mean geomagnetic field vector during the lock-in process. For a detailed description see Appendix A.

The solution to the ordinary differential equation in (5) is given by the function $\mathbf{m}_p \colon [\tau, \infty] \to \mathbb{R}^2$ with

$$\mathbf{m}_p(z) = \mathbf{b}(\tau)\mathrm{e}^{-\Gamma_{\tau,r_{p,\tau}}(t)} + \mathrm{e}^{-\Gamma_{\tau,r_{p,\tau}}(t)} \int_\tau^t \mathrm{e}^{\Gamma_{\tau,r_{p,\tau}}(t')} \gamma_{\tau,r_{p,\tau}}(t')\, \mathbf{b}(t')\, dt' \tag{6}$$

where $\Gamma_{\tau,r_{p,\tau}}(t) = \int_\tau^t \gamma_{\tau,r_{p,\tau}}(\rho) d\rho$ denotes the antiderivative of $\gamma_{\tau,r_{p,\tau}}$.

For a completely locked in particle, the function $\mathbf{m}_p$ is constant, since $\gamma_{\tau,r_{p,\tau}}(t) = 0$ for $t \geq \tau + r_{p,\tau}$ and its antiderivative is constant. Consequently, for $t \geq \tau + r_{p,\tau}$ the solution is constant and given by

$$\begin{aligned} \mathbf{m}_p(t) &= \mathbf{m}_p(\tau + r_{p,\tau}) \\ &= \mathbf{b}(\tau)\mathrm{e}^{-\Gamma_{\tau,r_{p,\tau}}(\tau + r_{p,\tau})} + \mathrm{e}^{-\Gamma_{\tau,r_{p,\tau}}(\tau + r_{p,\tau})} \int_\tau^{\tau + r_{p,\tau}} \mathrm{e}^{\Gamma_{\tau,r_{p,\tau}}(t')} \gamma_{\tau,r_{p,\tau}}(t')\, \mathbf{b}(t')\, dt' \end{aligned}$$

To summarize, we have derived an individual lock-in function for each particle of a given layer. Because of the sedimentation rate, these lock-in functions depend on the beginning of the lock-in process. A lower sedimentation rate causes a longer lock-in process, whereas a higher sedimentation rate causes a shorter lock-in process. However, we assume that the sediment layer thickness needed for complete consolidation does not change over time. We will thus formulate the previous results in terms of depth rather than time.

For this purpose, let $\varphi \colon \mathbb{R} \to \mathbb{R}$ be an age-depth model. Note that φ is a monotonically decreasing function that maps depths of the sediment core sample to ages. Here ages describes the time when the particle settled on the sediment-water interface. As described above the duration of the lock-in process depends on the time when the lock-in process began. However, the difference between the depth corresponding to the beginning of the lock-in process $\varphi^{-1}(\tau)$ and the depth corresponding to the end of the lock-in process $\varphi^{-1}(\tau + r_{p,\tau})$ is independent of the sedimentation rate and can be assumed to be constant (time independence of sediment layer thickness needed for complete consolidation). Consequently, for each particle p, we can find an $r_p \in \mathbb{R}$, such that

$$\varphi^{-1}(\tau + r_{p,\tau}) - \varphi^{-1}(\tau) = r_p \tag{7}$$

for all $\tau \in \mathbb{R}$. Therefore, we can formulate the function $\mathbf{m}_p$ in depth as

$$\tilde{\mathbf{m}}_p(z) = \mathrm{e}^{-\hat{\Gamma}_{r_p}(r_p)} \left(\tilde{\mathbf{b}}(z) + \int_0^{r_p} \mathrm{e}^{\hat{\Gamma}_{r_p}(z')} \hat{\gamma}_{r_p}(z') \tilde{\mathbf{b}}(z - z') dz' \right)$$

where $\hat{\gamma}_{r_p}$ denotes the shifted and depth dependent analogue to $\gamma_{\tau,r_{p,\tau}}$ and $\tilde{\mathbf{b}}$ is the depth dependent analogue to $\mathbf{b}$. A detailed derivation of this formula can be found in Appendix B.

In a next step, we extend this result to a whole layer of the sediment core with a collection of different particles. The different behaviors of these particles are described by their individual mobility functions. We assume that each of these mobility functions can be uniquely defined by $n \in \mathbb{N}$ shape parameters and their roots. Under this assumption, we can consider each mobility function as a realization of a random function $\hat{\gamma}_{S,R}$, where $S\colon \Omega \to \mathbb{R}^n$ and $R\colon \Omega \to \mathbb{R}$ are two random variables with probability density functions ϕ_S and ϕ_R. The root of each mobility function is a realization of the random variable R. The random variable S corresponds to the shape parameter of each mobility function.

All particles of a given layer must be locked in after a finite time period. Therefore, the support of the random variable R is bounded, i.e. we can find a $\lambda \in \mathbb{R}_{>0}$ such that $\mathrm{supp}(R) = [0, \lambda] \subset \mathbb{R}$. Here λ denotes the depth where the last particle of a given layer is fully locked in.

We set $\tilde{\mathbf{m}}\colon \mathbb{R}_{\geq 0} \to \mathbb{R}^2$ such that for each depth $z \in \mathbb{R}_{\geq 0}$

$$\begin{aligned}
\tilde{\mathbf{m}}(z) &= \mathbb{E}_{S,R}\left[\mathrm{e}^{-\hat{\Gamma}_{S,R}(R)}\left(\tilde{\mathbf{b}}(z) + \int_0^R \mathrm{e}^{\hat{\Gamma}_{S,R}(z')}\hat{\gamma}_{S,R}(z')\tilde{\mathbf{b}}\left(z - z'\right)dz'\right)\right] \\
&= \mathbb{E}_{S,R}\left[\mathrm{e}^{-\hat{\Gamma}_{S,R}(R)}\left(\tilde{\mathbf{b}}(z) + \int_0^\lambda \mathrm{e}^{\hat{\Gamma}_{S,R}(z')}\hat{\gamma}_{S,R}(z')\tilde{\mathbf{b}}\left(z - z'\right)dz'\right)\right] \\
&= \mathbb{E}_{S,R}\left[\mathrm{e}^{-\hat{\Gamma}_{S,R}(R)}\int_0^\lambda \delta(z')\tilde{\mathbf{b}}\left(z - z'\right) + \mathrm{e}^{\hat{\Gamma}_{S,R}(z')}\hat{\gamma}_{S,R}(z')\tilde{\mathbf{b}}\left(z - z'\right)dz'\right] \\
&= \int_0^\lambda \tilde{\mathbf{b}}\left(z - z'\right)\mathbb{E}_{S,R}\left[\mathrm{e}^{-\hat{\Gamma}_{S,R}(R)}\left(\delta(z') + \mathrm{e}^{\hat{\Gamma}_{S,R}(z')}\hat{\gamma}_{S,R}(z')\right)\right]dz'
\end{aligned}$$

where δ denotes the Dirac-delta function and $\mathbb{E}_{S,R}$ denotes the expected value with respect to the random variables S and R, i.e. $\mathbb{E}_{S,R}[f(S,R)] = \int\int f(s,r)\phi_R(r)\phi_S(s)drds$.

For each $z \in \mathbb{R}_{\geq 0}$, $\tilde{\mathbf{m}}(z) \in \mathbb{R}^2$ is, by construction, a vector on the tangent plane of the unit sphere. By projecting $\tilde{\mathbf{m}}(z)$ back to the unit sphere, we end up with a vector $\mathbf{e}_{\tilde{\mathbf{M}}_{\mathrm{proj}}}(z) \in \mathbb{S}^2$ that is approximately the smoothed normalized magnetic moment of the layer at depth z, denoted by $\mathbf{e}_{\tilde{\mathbf{M}}}(z) \in \mathbb{S}^2$. Consequently, for each $z \in \mathbb{R}_{\geq 0}$ the normalized magnetic moment is given by

$$\mathbf{e}_{\tilde{\mathbf{M}}}(z) = \int_0^\lambda \mathbf{e}_{\tilde{\mathbf{B}}}\left(z - z'\right)\mathbb{E}_{S,R}\left[\mathrm{e}^{-\hat{\Gamma}_{S,R}(R)}\left(\delta(z') + \mathrm{e}^{\hat{\Gamma}_{S,R}(z')}\hat{\gamma}_{S,R}(z')\right)\right]dz'$$

To sum up, we derived a lock-in function $F\colon \mathbb{R}_{\geq 0} \to \mathbb{R}_{\geq 0}$ defined over depth and given by

$$F(z) = \mathbb{E}_{S,R}\left[\mathrm{e}^{-\hat{\Gamma}_{S,R}(R)}\left(\delta(z) + \mathrm{e}^{\hat{\Gamma}_{S,R}(z)}\hat{\gamma}_{S,R}(z)\right)\right]$$

Note that this lock-in function is independent of the absolute depth and can therefore be applied to each layer of the sediment core sample. To achieve this independence we had to approximate the intensity of the geomagnetic field by a constant. Consequently, the derived lock-in function can only be used as a weight function for the directional components. A lock-in function for intensities can, in general, not be independent of absolute depth or absolute time.

The derived lock-in function is by construction normalized, i.e.

$$\int_0^\lambda F(z')dz' = 1 \tag{8}$$

The lock-in function depends on the distribution of the random variables S and R as well as on the mobility function $\hat{\gamma}_{S,R}$ and therefore also on the dimension of the random variable S. These parameters are influenced by the individual parameter distributions of the sediment core sample, e.g. distribution of grain size, shape, magnetic material etc.

However, there are two primary limitations that prevent us from proceeding with this general lock-in function. Firstly, the available information on sediment core samples is typically incomplete, lacking essential details. Secondly, even if we were to assume a meticulously investigated sediment core sample with all necessary information, the impact of individual sediment core sample parameters on the mobility function remains uncertain. To address these challenges, we adopt the following approximation: we fix the number of shape parameters and obtain an explicit form of the mobility function.

We assume that each particle's mobility decreases linearly with depth. Each linear function is uniquely characterized by its slope and its root. Therefore, the random variable S becomes 1-dimensional and the mobility functions of the particles are realizations of the following random function and its antiderivative

$$\hat{\gamma}_{S,R}(z) = \max\{S(R-z), 0\}$$
$$\hat{\Gamma}_{S,R}(z) = \min\left\{S\left(Rz - \frac{1}{2}z^2\right), \frac{1}{2}SR^2\right\}$$

In a next step we investigate how the shape of the lock-in function changes under different distributions of the random variables S and R. We conclude that, although the distribution of S heavily influences the shape of the individual lock-in functions, the influence on the shape of the general lock-in function can be neglected.

Motivated by these results, we set $S = 1$ for each mobility function and get for the random mobility function and its antiderivative

$$\hat{\gamma}_{R}(z) = \max\{R-z, 0\}$$
$$\hat{\Gamma}_{R}(z) = \min\left\{Rz - \frac{1}{2}z^2, \frac{1}{2}R^2\right\}$$

The general lock-in function is then given by

$$F(z) = \mathbb{E}_R\left[\mathrm{e}^{-\frac{1}{2}R^2}\left(\delta(z) + \mathrm{e}^{Rz-\frac{1}{2}z^2}\max\{R-z,0\}\right)\right] \tag{9}$$

In a final step we approximate this function by the following piecewise linear parameterized function

$$F_{b_1,b_2,b_3,b_4}(z) = \frac{2}{-b_1-b_2+b_3+b_4}\begin{cases} 0 & z \le b_1 \\ \frac{z-b_1}{b_2-b_1} & b_1 < z \le b_2 \\ 1 & b_2 < z \le b_3 \\ \frac{b_4-z}{b_4-b_3} & b_3 < z \le b_4 \\ 0 & b_4 \le z \end{cases} \tag{10}$$

Depending on the four parameters $b_1, b_2, b_3, b_4 \in \mathbb{R}_{\ge 0}$ with $b_1 \le b_2 \le b_3 \le b_4$, the parameterized function F_{b_1,b_2,b_3,b_4} can approximate possible lock-in functions.

In Figure 2 results for four different distributions of the random variable R are visualized. The lock-in depths of the individual particles are (**A**) uniformly distributed over the interval $[0, 10]$, (**B**) exponentially distributed with rate parameter 0, (**C**) normally distributed with mean 8 and variance 1, (**D**) exponentially distributed with rate parameter 2. In each case, one thousand individual lock-in functions are plotted (gray). These individual lock-in functions where used to approximate the expected value associated with the general lock-in function (orange). Finally, non-linear least squares is used to fit the parameterized lock-in function (green) to the general lock-in function.

The code to investigate additional examples can be found on our website under https://sec23.git-pages.gfz-potsdam.de/korte/pdrm/.

2.3 Data Model

In this section we will derive the data model which describes the relation between the measured signal in the sedimentary records and the geomagnetic field variations. While

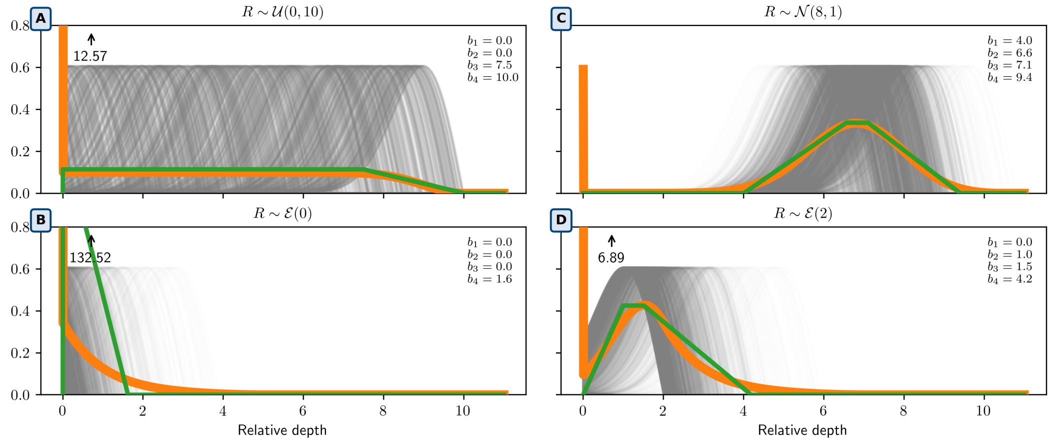

Figure 2. Individual lock-in functions of one thousand particles (gray), associated general lock-in function (orange) and fitted parameterized lock-in function (green) for four different distributions of the random variable R.

our primary focus here is on the sedimentary records, we need the information from archaeological records at a later stage. The model of archeological data is outlined in Schanner et al. (2022).

The first functional, used to describe the data model, is associated with the smoothing caused by the lock-in process and given by

$$\mathfrak{F}_z : \mathcal{C}(\mathbb{R}, \mathbb{R}^3) \to \mathbb{R}^3 \qquad \Big(z \mapsto \mathbf{G}(z)\Big) \mapsto \int_0^\lambda \frac{\mathbf{G}(z - z')}{\bar{\mathrm{B}}} F(z') dz'$$

where $F : \mathbb{R} \to \mathbb{R}$ is the lock-in function defined in section 2.2 and $\lambda > 0$ is the lock-in depth, i.e. the relative depth where the last particle of the layer at depth z is fully locked in. The constant $\bar{\mathrm{B}}$ is the mean of the geomagnetic field intensity over the absolute time of the sediment core sample, defined in section 2.2. We have to divide by $\bar{\mathrm{B}}$ since the lock-in function is defined for the directional components only. The linearity of the functional $\mathfrak{F}$ follows directly from the linearity of the integral.

Besides the natural smoothing caused by the lock-in process there is a smoothing effect caused by the way the magnetization in a sediment core sample is measured. When investigating sediment core samples, cubes of different sizes are taken from the core. Afterwards, the magnetization in the extracted cube is measured. The resulting measurement is then an average of the actual magnetization across the width of the cube. We assume that the size of the extracted cubes does not change within a core sample i.e. the size of the extracted cube does not depend on the depth where the cube is extracted. Therefore, we can define the size of the extracted cubes for one core sample as $\kappa \in \mathbb{R}_{>0}$.

This results in a second smoothing and can be described by the following measurement smoothing functional

$$\mathfrak{M}_z : \mathcal{C}(\mathbb{R}, \mathbb{R}^3) \to \mathbb{R}^3 \qquad \Big(z \mapsto \mathbf{G}(z)\Big) \mapsto \frac{1}{\kappa} \int_{z-\frac{\kappa}{2}}^{z+\frac{\kappa}{2}} \mathbf{G}(z') dz' \; .$$

The linearity of the functional $\mathfrak{M}$ again follows from the linearity of the integral.

As described in Schanner et al. (2022), the quantities that are measured in laboratory experiments are not provided in Cartesian field vector components (North (N), East (E), Down (Z)) but as two angles, declination (D) and inclination (I), and intensity (F). The non-linear relationships between these components can be described by three observation functionals

$$\begin{aligned}
\mathfrak{H}_z^D \colon \mathcal{C}(\mathbb{R},\mathbb{R}^3) \to \mathbb{R}^3 \qquad & \Big(z \mapsto \mathbf{G}(z)\Big) \mapsto \arctan\left(\frac{\mathrm{G}_E(z)}{\mathrm{G}_N(z)}\right) \\
\mathfrak{H}_z^I \colon \mathcal{C}(\mathbb{R},\mathbb{R}^3) \to \mathbb{R}^3 \qquad & \Big(z \mapsto \mathbf{G}(z)\Big) \mapsto \arctan\left(\frac{\mathrm{G}_Z(z)}{\sqrt{\mathrm{G}_N^2(z) + \mathrm{G}_E^2(z)}}\right) \\
\mathfrak{H}_z^F \colon \mathcal{C}(\mathbb{R},\mathbb{R}^3) \to \mathbb{R}^3 \qquad & \Big(z \mapsto \mathbf{G}(z)\Big) \mapsto \sqrt{\mathrm{G}_E^2(z) + \mathrm{G}_N^2(z) + \mathrm{G}_Z^2(z)}
\end{aligned}$$

where $\mathbf{G}(z) = \begin{pmatrix}\mathrm{G}_N(z) & \mathrm{G}_E(z) & \mathrm{G}_Z(z)\end{pmatrix}^\top \in \mathbb{R}^3$ for each $z \in \mathbb{R}$.

In the following we will apply these functionals to the Gaussian Process associated with the geomagnetic field. Note that the lock-in function is defined in depth. Therefore, we can not directly use the time dependent Gaussian Process given in (1). By switching from time to depth we end up with a new Gaussian Process

$$\tilde{\mathbf{B}} \sim \mathcal{GP}\left(\bar{\mathbf{B}}, K_{\tilde{\mathbf{B}}}\right)$$

where the mean function coincides with the mean function of the Gaussian Process given in (1). This is because the mean function is assumed to be constant. The kernel function follows directly by applying the age-depth model to the kernel function of the Gaussian Process given in (1).

By applying the functional $\mathfrak{F}$ to the Gaussian process $\tilde{\mathbf{B}}$, we get, for all $z \in \mathbb{R}$, the first part of our data model

$$\mathbf{o}_1(z) = \mathfrak{F}_z\left[\tilde{\mathbf{B}}\right] = \int_0^\lambda \frac{\tilde{\mathbf{B}}(z-z')}{\bar{\mathrm{B}}} F(z')dz' \; .$$

Since $\tilde{\mathbf{B}}$ is a Gaussian Process and by the linearity of the functional $\mathfrak{F}$ it follows that also $\mathbf{o}_1$ is a Gaussian Process.

Applying the measurement functional $\mathfrak{M}$ to the data model $\mathbf{o}_1$, leads, for all $z \in \mathbb{R}$, to a new data model

$$\mathbf{o}_2(z) = \mathfrak{M}_z[\mathbf{o}_1] = \frac{1}{\kappa} \int_{z-\frac{\kappa}{2}}^{z+\frac{\kappa}{2}} \mathbf{o}_1(z'')dz'' \; .$$

Note that $\mathbf{o}_2$ is also a Gaussian Process.

Assuming that the lock-in depth λ is significantly larger than the size of the sample cube κ, the measurement smoothing is negligible. In other words we can approximate $\mathbf{o}_2$ by $\mathbf{o}_1$, i.e. $\mathbf{o}_2(z) \approx \mathbf{o}_1(z)$.

By applying the three non-linear functionals $\mathfrak{H}^D$, $\mathfrak{H}^I$ and $\mathfrak{H}^F$ to the data model $\mathbf{o}_2$, we get a new data model consisting, for all $z \in \mathbb{R}$, of the following three components

$$\mathbf{o}_3^D(z) = \mathfrak{H}_z^D[\mathbf{o}_2], \quad \mathbf{o}_3^I(z) = \mathfrak{H}_z^I[\mathbf{o}_2], \quad \mathbf{o}_3^Z(z) = \mathfrak{H}_z^F[\mathbf{o}_2]$$

The non-linearity results in a data model that is not Gaussian anymore. However, as described in Schanner et al. (2022), these functionals can be linearized by a first order Taylor expansion. As the point of expansion we use the smoothed mean of the Gaussian process associated with the geomagnetic field

$$\mathfrak{F}_z\left[\bar{\mathbf{B}}\right] = \int_0^\lambda \frac{\bar{\mathbf{B}}(z-z')}{\bar{\mathrm{B}}} F(z')dz' = \frac{\bar{\mathbf{B}}}{\bar{\mathrm{B}}} \int_0^\lambda F(z')dz' = \frac{\bar{\mathbf{B}}}{\bar{\mathrm{B}}}$$

where $\bar{\mathbf{B}} = \begin{pmatrix}\bar{\mathrm{B}}_N & \bar{\mathrm{B}}_E & \bar{\mathrm{B}}_Z\end{pmatrix}^\top \in \mathbb{R}^3$.

The linearization results in three functionals ${\mathfrak{H}_{\mathrm{lin}}}_z^D, {\mathfrak{H}_{\mathrm{lin}}}_z^I, {\mathfrak{H}_{\mathrm{lin}}}_z^F : \mathcal{C}(\mathbb{R}, \mathbb{R}^3) \to \mathbb{R}^3$ such that for $\mathbf{G} \in \mathcal{C}(\mathbb{R}, \mathbb{R}^3)$

$$
\begin{aligned}
{\mathfrak{H}_{\mathrm{lin}}}_z^D[\mathbf{G}] &= \bar{\mathrm{B}}_D + \frac{\bar{\mathrm{B}}}{\tilde{F}_H^2} \begin{pmatrix} -\bar{\mathrm{B}}_E \\ \bar{\mathrm{B}}_N \\ 0 \end{pmatrix}^\top \mathbf{G}(z) \\
{\mathfrak{H}_{\mathrm{lin}}}_z^I[\mathbf{G}] &= \bar{\mathrm{B}}_I + \frac{\bar{\mathrm{B}}}{\tilde{F}_H} \left(\begin{pmatrix} 0 \\ 0 \\ 1 \end{pmatrix} - \frac{\bar{\mathrm{B}}_Z}{\tilde{F}} \frac{\bar{\mathbf{B}}}{\tilde{F}} \right)^\top \mathbf{G}(z) \\
{\mathfrak{H}_{\mathrm{lin}}}_z^F[\mathbf{G}] &= \frac{\bar{\mathbf{B}}^\top}{\tilde{F}} \mathbf{G}(z)
\end{aligned}
$$

where $\tilde{F} = \sqrt{\bar{\mathrm{B}}_N^2 + \bar{\mathrm{B}}_E^2 + \bar{\mathrm{B}}_Z^2}$, $\tilde{F}_H = \sqrt{\bar{\mathrm{B}}_N^2 + \bar{\mathrm{B}}_E^2}$.

By using these linearized functionals we approximate the data model $\mathbf{o}_3$ by a Gaussian Process.

In conclusion the components of our final data model are given by

$$
\begin{aligned}
\mathbf{o}^D(z) &= \mathbf{o}_3^D(z) + \mathrm{E}^D(z) \\
&= \mathfrak{H}_z^D\left[\mathbf{o}_2\right] + \mathrm{E}^D(z) \\
&= \mathfrak{H}_z^D\left[\frac{1}{\kappa}\int_{z-\frac{\kappa}{2}}^{z+\frac{\kappa}{2}} \mathbf{o}_1(z'')dz''\right] + \mathrm{E}^D(z) \\
&= \mathfrak{H}_z^D\left[\frac{1}{\kappa}\int_{z-\frac{\kappa}{2}}^{z+\frac{\kappa}{2}} \int_0^\lambda \frac{\tilde{\mathbf{B}}(z''-z')}{\bar{B}} F(z')dz'dz''\right] + \mathrm{E}^D(z) \\
&\approx \mathfrak{H}_z^D\left[\int_0^\lambda \frac{\tilde{\mathbf{B}}(z-z')}{\bar{B}} F(z')dz'\right] + \mathrm{E}^D(z) \\
&\approx {\mathfrak{H}_{\mathrm{lin}}}_z^D\left[\int_0^\lambda \frac{\tilde{\mathbf{B}}(z-z')}{\bar{B}} F(z')dz'\right] + \mathrm{E}^D(z) \\
&= \bar{\mathrm{B}}_D + \frac{1}{\tilde{F}_H^2} \begin{pmatrix} -\bar{\mathrm{B}}_E \\ \bar{\mathrm{B}}_N \\ 0 \end{pmatrix}^\top \int_0^\lambda \tilde{\mathbf{B}}(z-z')F(z')dz' + \mathrm{E}^D(z) \\
\mathbf{o}^I(z) &\approx \bar{\mathrm{B}}_I + \frac{1}{\tilde{F}_H} \left(\begin{pmatrix} 0 \\ 0 \\ 1 \end{pmatrix} - \frac{\bar{\mathrm{B}}_Z}{\tilde{F}} \frac{\bar{\mathbf{B}}}{\tilde{F}} \right)^\top \int_0^\lambda \tilde{\mathbf{B}}(z-z')F(z')dz' + \mathrm{E}^I(z) \\
\mathbf{o}^F(z) &\approx \frac{1}{\bar{\mathrm{B}}^2 \bar{\mathrm{B}}_F} \bar{\mathbf{B}}^\top \int_0^\lambda \tilde{\mathbf{B}}(z-z')F(z')dz' + \mathrm{E}^F(z)
\end{aligned}
$$

where $\mathbf{E} = \begin{pmatrix} \mathrm{E}_N & \mathrm{E}_E & \mathrm{E}_Z \end{pmatrix}^\top \in \mathbb{R}^3$ indicates the vector of measurement errors.

2.4 Sequentialization

Similar to Schanner et al. (2022) we perform a sequentialized inversion. We use the same archaeomagnetic data as in Schanner et al. (2022) and, for now, sediment data from a single sediment core only. In a later version we will adjust the method such that multiple sediment core samples can be used. We restrict the set of free hyperparameters to the four shape parameters of the parameterized lock-in function in (10). For the hyperparameters of the geomagnetic field prior, we use the values estimated in Schanner et al. (2022). In other words, we use the archaeomagnetic data to estimate the shape of the lock-in function. Due to the temporal distribution of the archaeomagnetic data, we recommend limiting the time period for the hyperparameter estimation to the last eight thousand years.

We perform a modified version of the Kalman filter inversion (Kalman, 1960) presented in Baerenzung et al. (2020); Schanner et al. (2022). In each step, the Kalman filter consists of a prediction step followed by a correction step with respect to the new data if available. The correction step updates the model which is then used for the prediction in the next step. By setting a cutoff degree $l_{\max}$, the model can be described by a finite vector of Gauss coefficients and their derivatives $\mathbf{z} = (g_l^m, \dot{g}_l^m)$.

In Schanner et al. (2022) a cutoff degree of $l_{\max} = 20$ is used. Together with a step size of $\Delta t = 10$ yrs, this provides a resolution that is much higher than the resolution given by the available data. Due to computational reasons we have to decrease the cutoff degree to $l_{\max} = 8$ and the step size to $\Delta t = 40$ yrs. However, several tests showed that the resolution is still high enough to capture all information provided by the available data.

We cannot directly use the prediction and correction step formulas presented in Baerenzung et al. (2020). Because of the lock-in process, the prediction and correction in each step depends conditionally on the data contained in the maximal lock-in depth n. We overcome the dependence problem by considering explicit correlation between a finite number of Kalman filter stepts, corresponding to the maximal lock-in depth n. For each $k \in [0, T]$, where $T > n$ denotes the number of total Kalman filter steps, this leads to a forward operator defined as

$$\mathbf{F}_k = \mathbf{F}_k(l_{\max}, \Delta t) = \begin{pmatrix} \mathrm{F}_k & \mathbf{0}_{1,n-1} \\ \mathbf{1}_{n-1,n-1} & \mathbf{0}_{n-1,n} \end{pmatrix}$$

where $\mathrm{F}_k = \mathrm{F}_k(l_{\max}, \Delta t)$ is the forward operator defined in Baerenzung et al. (2020). Since we have chosen a constant step size, the forward operator does not depend on the Kalman filter step, i.e. $\mathbf{F}_k = \mathbf{F}$ for all k.

The notation $\mathbf{0}_{a,b}$ and $\mathbf{1}_{a,b}$ denote the $a \times b$ dimensional zero and identity matrix, respectively. Note that F_k is an $2l_{\max}(l_{\max}+2) \times 2l_{\max}(l_{\max}+2)$ matrix itself. Therefore, $\mathbf{F}_k$ is an $n \times n$ matrix with $2l_{\max}(l_{\max}+2) \times 2l_{\max}(l_{\max}+2)$ matrices as entries.

Let $\mathbf{z}_0 \sim \mathcal{N}(\boldsymbol{\mu}_0, \boldsymbol{\Sigma}_0)$ be the prior, where $\boldsymbol{\mu}_0$ and $\boldsymbol{\Sigma}_0$ are the prior mean and covariance matrices, respectively. For $k \in [1, T]$, the Bayesian filtering equations are recursively defined as

$$\begin{aligned} \mathbf{z}_k &= \mathbf{F}\mathbf{z}_{k-1} + \boldsymbol{\sigma} \\ \mathbf{o}_k &= \mathbf{H}_k \mathbf{z}_k + \mathbf{e}_k \end{aligned}$$

where $\mathbf{o}_k$ is the measurement, $\boldsymbol{\sigma} \sim \mathcal{N}(\mathbf{0}, \boldsymbol{\Sigma})$ the process noise and $\mathbf{e}_k \sim \mathcal{N}(\mathbf{0}, \mathbf{E}_k)$ the measurement noise. The matrix $\mathbf{H}_k$ is the operator that projects the model to the data. The matrix $\tilde{\boldsymbol{\Sigma}} = \boldsymbol{\Sigma}_0 - \mathbf{F}\boldsymbol{\Sigma}_0\mathbf{F} = \begin{pmatrix} \tilde{\Sigma} & \mathbf{0}_{1,n-1} \\ \mathbf{0}_{n-1,n-1} & \mathbf{0}_{n-1,n} \end{pmatrix}$ characterizes the white noise of the evolution model. It is independent of the Kalman filter step because of stationarity.

For $1 \leq a < b \leq n$ and $1 \leq c < d \leq m$ and an $n \times m$ matrix $\mathbf{A}$ we denote by $\mathbf{A}^{a:b,c:d}$ the matrix entries with row indices between a and b and column indices between c and d.

For $k \in [1, T]$ and with the modified forward operator, the recursive equations of the prediction step are given by

$$\begin{aligned} \boldsymbol{\mu}_k^- &= \mathbf{F}\boldsymbol{\mu}_{k-1} = \begin{pmatrix} \mathrm{F}\boldsymbol{\mu}_{k-1}^1 \\ \boldsymbol{\mu}_{k-1}^{1:n-1} \end{pmatrix} \\ \boldsymbol{\Sigma}_k^- &= \mathbf{F}\boldsymbol{\Sigma}_{k-1}\mathbf{F}^\top + \tilde{\boldsymbol{\Sigma}} = \begin{pmatrix} \mathrm{F}\boldsymbol{\Sigma}_{k-1}^{1,1}\mathrm{F}^\top + \tilde{\Sigma} & \mathrm{F}\boldsymbol{\Sigma}_{k-1}^{1,1:n-1} \\ \boldsymbol{\Sigma}_{k-1}^{1:n-1,1}\mathrm{F}^\top & \boldsymbol{\Sigma}_{k-1}^{1:n-1,1:n-1} \end{pmatrix} . \end{aligned}$$

The recursive equations for the update step are given by

$$\begin{aligned}
\mathbf{S}_k &= \mathbf{H}_k \boldsymbol{\Sigma}_k^- \mathbf{H}_k^\top + \mathbf{E}_k \\
\mathbf{K}_k &= \boldsymbol{\Sigma}_k^- \mathbf{H}_k^\top \mathbf{S}_k^{-1} \\
\boldsymbol{\mu}_k &= \boldsymbol{\mu}_k^- + \mathbf{K}_k \left(\mathbf{o}_k - \mathbf{H}_k \boldsymbol{\mu}_k^-\right) \\
\boldsymbol{\Sigma}_k &= \boldsymbol{\Sigma}_k^- - \mathbf{K}_k \mathbf{S}_k \mathbf{K}_k^\top \ .
\end{aligned}$$

To formulate the backward recursion equations assume that the recursion starts from the last time step T. We set $\boldsymbol{\mu}_T^s = \boldsymbol{\mu}_T$ and $\boldsymbol{\Sigma}_T^s = \boldsymbol{\Sigma}_T$.

The backward recursion equations are given as

$$\begin{aligned}
\boldsymbol{\mu}_{k+1}^- &= \mathbf{F}\boldsymbol{\mu}_k = \begin{pmatrix} \mathrm{F}\boldsymbol{\mu}_k^1 \\ \boldsymbol{\mu}_k^{1:n-1} \end{pmatrix} \\
\boldsymbol{\Sigma}_{k+1}^- &= \mathbf{F}\boldsymbol{\Sigma}_k\mathbf{F}^\top + \tilde{\boldsymbol{\Sigma}} = \begin{pmatrix} \mathrm{F}\boldsymbol{\Sigma}_k^{1,1}\mathrm{F}^\top + \tilde{\Sigma} & \mathrm{F}\boldsymbol{\Sigma}_k^{1,1:n-1} \\ \boldsymbol{\Sigma}_k^{1:n-1,1}\mathrm{F}^\top & \boldsymbol{\Sigma}_k^{1:n-1,1:n-1} \end{pmatrix} \\
\mathbf{G}_k &= \boldsymbol{\Sigma}_k\mathbf{F}^\top(\boldsymbol{\Sigma}_{k+1}^-)^{-1} = \begin{pmatrix} \mathbf{0}_{n-1,1} & \mathbf{1}_{n-1,n-1} \\ \mathbf{0}_{1,1} & \underbrace{\boldsymbol{\Sigma}_k^{n,1:n-1}\left(\boldsymbol{\Sigma}_k^{1:n-1,1:n-1}\right)^{-1}}_{=\mathbf{A}_k \in \mathbb{R}^{1\times n-1}} \end{pmatrix} \\
\boldsymbol{\mu}_k^s &= \boldsymbol{\mu}_k + \mathbf{G}_k\left(\boldsymbol{\mu}_{k+1}^s - \boldsymbol{\mu}_{k+1}^-\right) = \begin{pmatrix} \boldsymbol{\mu}_{k+1}^{s,2:n-1} \\ \boldsymbol{\mu}_k^n + \mathbf{A}_k\left(\boldsymbol{\mu}_{k+1}^{s,2:n} - \boldsymbol{\mu}_k^{1:n-1}\right) \end{pmatrix} \\
\boldsymbol{\Sigma}_k^s &= \boldsymbol{\Sigma}_k + \mathbf{G}_k\left(\boldsymbol{\Sigma}_{k+1}^s - \boldsymbol{\Sigma}_{k+1}^-\right)\mathbf{G}_k^\top \\
&= \begin{pmatrix} \boldsymbol{\Sigma}_{k+1}^{s,2:n,2:n} & \boldsymbol{\Sigma}_{k+1}^{s,2:n,2:n}\mathbf{A}_k^\top \\ \mathbf{A}_k\boldsymbol{\Sigma}_{k+1}^{s,2:n,2:n} & \boldsymbol{\Sigma}_k^{n,n} + \mathbf{A}_k\left(\boldsymbol{\Sigma}_{k+1}^{s,2:n,2:n} - \boldsymbol{\Sigma}_k^{1:n-1,1:n-1}\right)\mathbf{A}_k^\top \end{pmatrix} \ .
\end{aligned}$$

A detailed derivation of these formulas can be found in Appendix C.

3 Results

In this section, we will assess the proposed method by conducting synthetic tests and applying it to two lake sediment records from Sweden. The data utilized in this section, along with the method's implementation, can be found on our website under https://sec23.git-pages.gfz-potsdam.de/korte/pdrm/ and in the corresponding GitLab repository (Bohsung & Schanner, 2023). Moreover, we have provided scripts for generating synthetic data, enabling further testing.

3.1 Synthetic Data

We tested the performance of our model on synthetic data. All synthetic data points are based on the same reference geomagnetic field time series drawn from the prior described in section 2.1. Three synthetic datasets where generated from this reference time series. The first dataset represents the archaeomagnetic data with input locations and times being the same as in the archaeomagnetic data used in Schanner et al. (2022). In addition, two synthetic sediment datasets where generated. One is located in Sweden (60°9′3.6″ N, 13°3′18″ E) and is denoted by sed_sweden. The other one, sed_rapa, is located on Rapa Iti (27°36′57.6″ S, 144°16′58.8″ W). Both have the same temporal distribution (see Appendix D Figure D1). The age-depth model used for both synthetic sediment data sets coincides with the age depth model of the lake sediment core KLK described in section 3.2.

We then applied four different lock-in functions to sed_sweden and sed_rapa, using the lock-in function in Equation (9) based on the lock-in depth distribution of the individual particles instead of the parameterized lock-in function in Equation (10). We used the four orange lock-in functions illustrated in Figure 2. Since our model does not directly infer these lock-in functions but the parameterized lock-in function given in (10), it is not a perfect inverse problem.

The results for sed_sweden (**A**)-(**C**) and sed_rapa (**D**)-(**F**) distorted with the lock-in function associated with the normal distribution are given in Figure 3. Panels (**A**) and (**D**) show comparisons of the lock-in function used to distort the data and the resulting estimated parameterized lock-in function (blue). The estimated parameters $b_1, \ldots, b_4$ are given in the legend. The upper panels in (**B**) and (**E**) show the reference time series (green) which was used to generate the archaeological and sediment data before the distortion. Additionally, the resulting posterior mean (blue) and one hundred samples from the posterior (blue with small opacity) for declination are shown. The upper panels of (**C**) and (**F**) show the same for inclination. The lower panels show the distorted sediment data with errors (orange), i.e. the input data. In addition, the resulting predicted sediment observations (purple) are shown. They are generated by applying the estimated parameterized lock-in functional to the posterior and the one hundred samples.

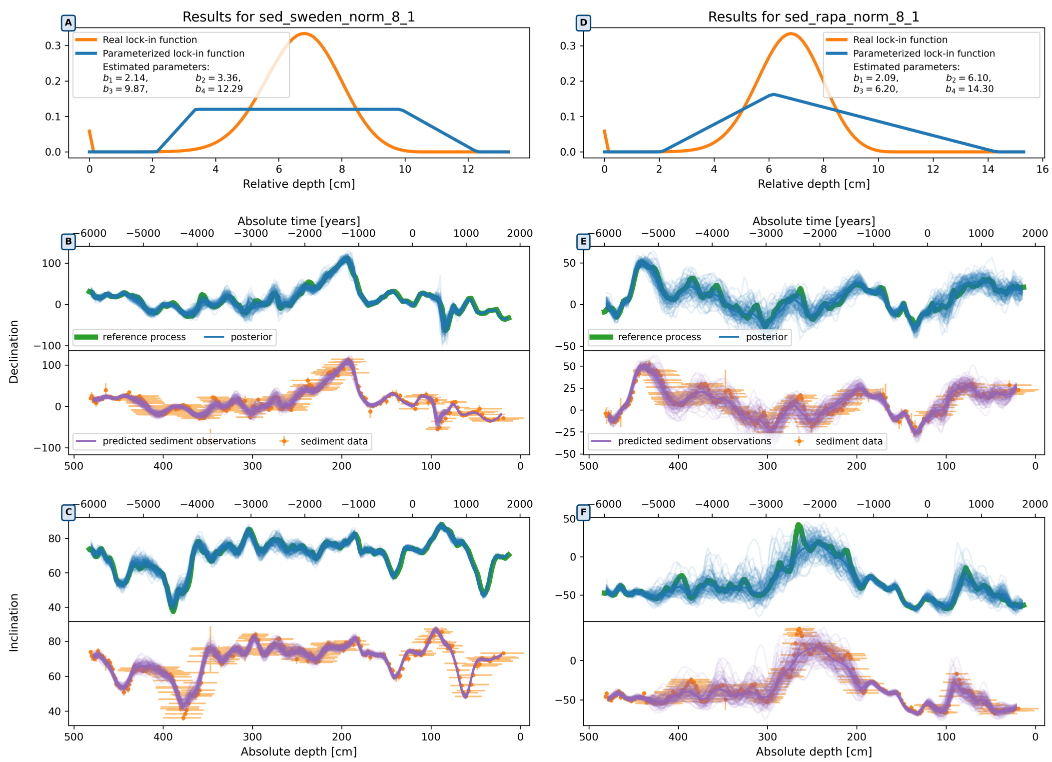

Figure 3. Results of modeling the pDRM for sed_sweden (left) and sed_rapa (right). Synthetic data are created from a reference process (green, (**B**) and (**E**) declination, (**C**) and (**F**) inclination) and distorted with the lock-in function (orange function in **A** and **D**) to form an input data series with uncertainties (orange points). Application of our lock-in model gives the posterior mean and 100 samples (blue in **B**, **C**, **E**, **F**) and estimated lock-in functions (blue in **A**, **B**). The mean and 100 samples of the posterior curves modified by the estimated lock-in function are also shown (purple in **B**, **C**, **E**, **F**).

For the results of the remaining three cases see Appendix D. Consistent outcomes are observed across all examined cases. Notably, even in instances where the approximation of the lock-in function used for the distortion is not ideal, the posterior distributions and predicted sediment observations exhibit remarkable accuracy.

Figure 4 shows the comparison of two posteriors, for the locations of (**A**) sed_sweden and (**B**) sed_rapa. The green curve shows the reference process, from which the synthetic data used here were created. Posterior mean and one hundred samples of a model inverted with archaeological data only (pink) and one inverted with archaeological and sediment data (blue) are shown for the declination (upper panels) and inclination (lower panels). The results for sed_sweden agree closely. For sed_rapa one can observe an improvement in the model inverted with sediment and archaeological records.

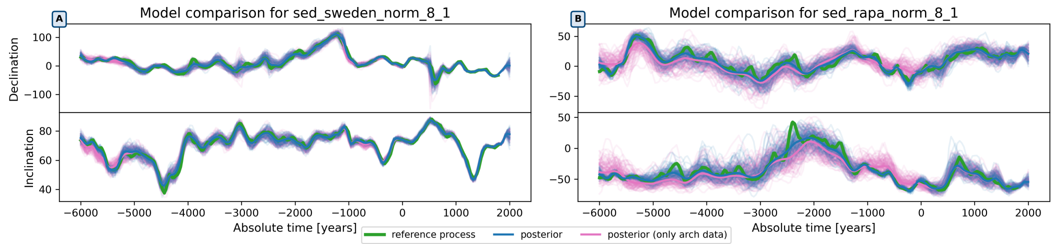

Figure 4. Posterior comparison of models based on archaeological data only (pink) and archaeological and sediment data (blue). In both cases the mean and 100 samples are shown. In green is the reference process, used to generate the synthetic data.

The results for the remaining three cases are similar. Please visit our website (https://sec23.git-pages.gfz-potsdam.de/korte/pdrm/) to see the remaining results.

3.2 Real Data

The proposed method is applied to two lake sediment cores located in Sweden, namely Kälksjön (KLK) (Stanton et al., 2010, 2011; Mellström et al., 2015) and Gyltigesjön (GYL) (Snowball et al., 2013; Mellström et al., 2013, 2015) as first test cases. Both records are composed of more than one core sample, which may lead to inconsistencies due to rotations or inaccurate samplings of the cores. In Nilsson et al. (2022) a binning method is used to eliminate these effects. We followed the same approach and generated two datasets KLK_binned and GYL_binned. However, we apply our method to both the original and the binned records.

The age-depth model used in this study is based on the posterior mean visualized in the appendix of Nilsson et al. (2022). Age uncertainties for KLK are set to 300 years, except for the two areas with radiocarbon dating where age uncertainties are set to 5 years. Similar, age uncertainties of the radiocarbon dated areas of GYL are set to 5 years. For records older than 1000 yr BCE and younger than 300 yr BCE, the age uncertainties are set to 200 years and 300 years, respectively. A more accurate age-depth model will be used in a future study.

The results for KLK are presented in Figure 5. (**A**)-(**C**) show the results for the raw data and (**D**)-(**F**) show the results for the binned data. The figure is organized as Figure 3, but reference curve and real lock-in function are now unknown, and the orange symbols are the real data with uncertainty estimates. The results regarding the estimated lock-in functions clearly differ whether the original or binned data were used, while the estimated posterior curves are very similar most of the time, except for declination around 1000 yr BCE.

The similar results for GYL are given in Appendix D in Figure D5.

4 Discussion

The strongest assumption in the modeling of the lock-in process is the constancy of geomagnetic field intensity. As we have seen, this assumption does not play a major role for the directional components (declination and inclination), but impedes the application of our method for the relative paleointensity of the magnetic moment of a sed-

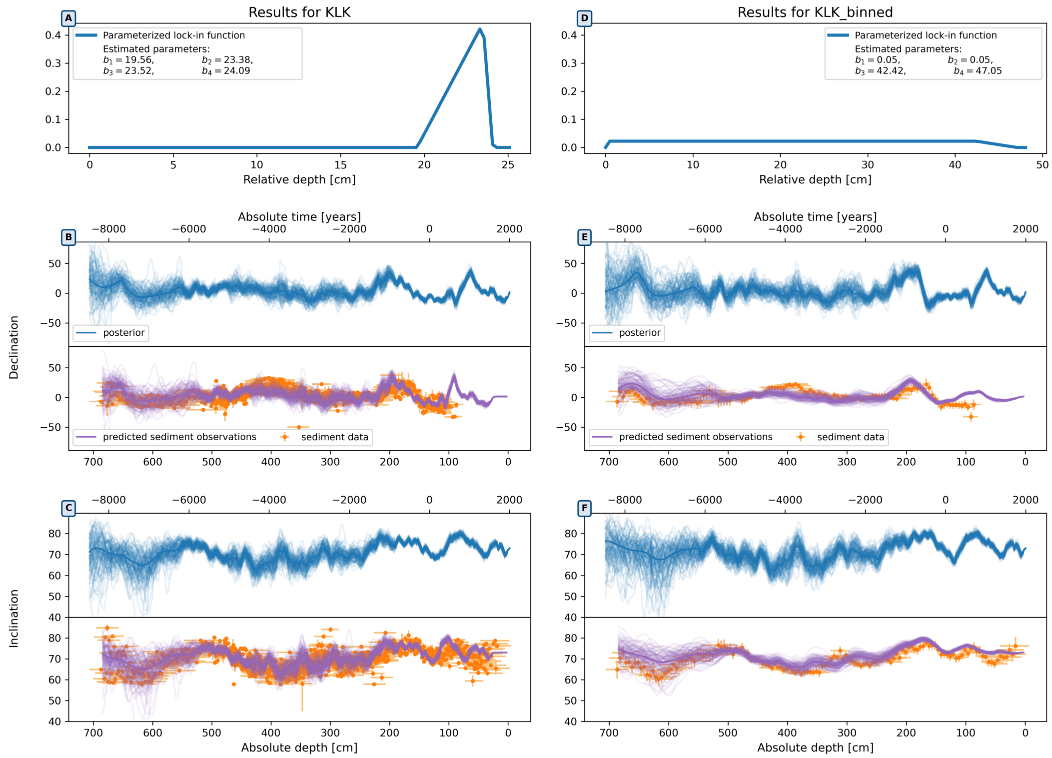

Figure 5. Results of modeling the pDRM for the real data series (orange symbols with uncertainty bars) KLK (**B**, declination and **C**, inclination) and KLK_binned (**E**, declination and **F**, inclination). Application of our lock-in model gives the posterior curves (**B**, **C**, **E**, **F**, blue, mean and 100 samples) and estimated lock-in functions (**A**, **B**, blue). The mean and 100 samples of the posterior curves modified by the estimated lock-in function are also shown in purple.

iment layer. The heuristic explanation is that while changes in geomagnetic intensity can alter the distribution of the lock-in times of individual particles, the surrounding material's influence is much more substantial, making this effect negligible. The correlations between the relative paleointensity and the intensity of the geomagnetic field are considerably more intricate. Further research will be required to explore these relationships. Another strong assumption was that the sedimentation material and its composition does not change significantly over time. Weakening of this assumption will be part of future research.

In contrast to various lock-in functions found in the literature, the parameterized lock-in function presented in this study can approximate all conceivable lock-in behaviors, including those that result in a shift. Higher degree functions or functions with more interpolation points could possibly yield better approximations, but would also increase the number of hyperparameters.

The synthetic tests conducted with sed_sweden show a remarkable fit of the posterior to the reference model in all cases, along with a good fit of the smoothed posterior to the smoothed synthetic sediment data. Notably, these positive results are achieved even when the parameterized lock-in function does not accurately approximate the true lock-in function. One possible explanation for this phenomenon is the non-uniqueness of the inversion performed, which we plan to investigate in more detail in a future study, including the uncertainties of the estimated parameters.

As expected, the results of the synthetic tests performed with sed_rapa appear somewhat inferior due to the scarcity of archaeological data in the vicinity of the sediment data. Nevertheless, the results are surprisingly good, especially in regions with small temporal errors. Additionally, the sediment records enhance the model prediction compared to the model inverted on archaeological records only.

Also, the application of the method to the KLK and GYL data sets yields promising results. It is remarkable that the binning, which is in principle an artificial smoothing, leads in both cases to a lock-in function which reproduces a strong smoothing. However, when we assess the fit of the smoothed posteriors to the actual data, the method does not perform as well as it did in the synthetic tests. This can be attributed to several reasons, including inconsistencies in the non-binned data, excessively small measurement errors, as well as high temporal errors. Moreover, the effects of inclination shallowing or rotations during core sampling have been disregarded, which may result in a variable fit of the smoothed posterior to either inclination or declination. The application of the method to a wider variety of real data will be investigated in more detail in a future study.

5 Conclusion

Through theoretical investigation, we have first studied the rotational dynamics of a single magnetic particle during the sedimentation process. Our findings demonstrate that, subject to several assumptions, a lock-in function that is independent of absolute parameters can only exist for the directional magnetic field components, but not for relative intensity. For these directional components, we derived a lock-in function for single particles, which was then generalized and approximated using a parameterized function. Extensive testing on synthetic data sets has demonstrated that our method is highly effective in eliminating pDRM effects. While the initial application to real data sets is promising, further investigation is required to fully evaluate its potential.

Appendix A

In this section, we'll demonstrate how the first order linear ordinary differential equation in (5) can approximate the differential equation in (4), for all $t \geq \tau$.

We set $\bar{\mathbf{e}}_\mathbf{B} = \frac{1}{r_{p,\tau}} \int_\tau^{\tau + r_{p,\tau}} \mathbf{e}_\mathbf{B}\,(t')\,dt' \in \mathbb{S}^3$ as the mean vector of all vectors corresponding to the geomagnetic field during the lock-in process. We choose the coordinate system in such a way, that the mean vector $\bar{\mathbf{e}}_\mathbf{B}$ points to the North Pole of the unit sphere. For each $t \in [\tau, \tau + r_{p,\tau})$, we project the three-dimensional vectors $\mathbf{e}_\mathbf{m}(t) \in \mathbb{R}^3$ and $\mathbf{e}_\mathbf{B}(t) \in \mathbb{R}^3$ perpendicular onto the tangent plane. This projection is given by $P\colon \mathbb{S}^2 \to \mathbb{R}^3$ with

$$P\left(\begin{pmatrix} x \\ y \\ z \end{pmatrix}\right) = \begin{pmatrix} x \\ y \\ 1 \end{pmatrix}$$

Alternatively, one can derive the projection as follows. For each $t \in [\tau, \tau + r_{p,\tau}]$ we project $\mathbf{e}_\mathbf{m}(t)$ via

$$P(\mathbf{e}_\mathbf{m}(t)) = \mathbf{e}_\mathbf{m}(t) + \lambda \bar{\mathbf{e}}_\mathbf{B}$$

with $\lambda \in \mathbb{R}$. We know that the projected vector on the tangent plane is orthogonal to $\bar{\mathbf{e}}_\mathbf{B}$. Hence,

$$\begin{aligned}
\langle \bar{\mathbf{e}}_\mathbf{B}, \mathbf{e}_\mathbf{m}(t) + \lambda \bar{\mathbf{e}}_\mathbf{B} \rangle = 0 &\Leftrightarrow \langle \bar{\mathbf{e}}_\mathbf{B}, \mathbf{e}_\mathbf{m}(t) \rangle + \lambda \langle \bar{\mathbf{e}}_\mathbf{B}, \bar{\mathbf{e}}_\mathbf{B} \rangle = 0 \\
&\overset{\|\bar{\mathbf{e}}_\mathbf{B}\|=1}{\Leftrightarrow} \langle \bar{\mathbf{e}}_\mathbf{B}, \mathbf{e}_\mathbf{m}(t) \rangle + \lambda = 0 \\
&\leftrightarrow \lambda = -\langle \bar{\mathbf{e}}_\mathbf{B}, \mathbf{e}_\mathbf{m}(t) \rangle
\end{aligned}$$

Therefore the projection is given by

$$P(\mathbf{e}_\mathbf{m}(t)) = \mathbf{e}_\mathbf{m}(t) - \langle \bar{\mathbf{e}}_\mathbf{B}, \mathbf{e}_\mathbf{m}(t) \rangle \bar{\mathbf{e}}_\mathbf{B}$$

By applying this projection to the vectors $\mathbf{e_m}(t)$ and $\mathbf{e_B}(t)$ we get for each $t \in [\tau, \tau + r_{p,\tau}]$

$$P(\mathbf{e_m}(t)) = \begin{pmatrix} \mathrm{m}_x(t) \\ \mathrm{m}_y(t) \\ 1 \end{pmatrix} = \begin{pmatrix} \mathbf{m}(t) \\ 1 \end{pmatrix} \quad \text{and} \quad P(\mathbf{e_B}(t)) = \begin{pmatrix} \mathrm{B}_x(t) \\ \mathrm{B}_y(t) \\ 1 \end{pmatrix} = \begin{pmatrix} \mathbf{b}(t) \\ 1 \end{pmatrix}$$

where $\mathbf{m}, \mathbf{b} \in \mathbb{R}^2$ are vectors on the tangent plane. By construction of the tangent plane, the choice of the coordinate system and under the assumption that the geomagnetic field only changes its direction by a few degrees in the time period $[\tau, \tau + r_{p,\tau}]$, the x- and y-components of the vectors $\mathbf{e_B}(t)$ are close to zero and the z-components are close to one. The same holds true for each vector $\mathbf{e_m}(t)$. Therefore, the approximation by the projection on the tangent plane is justified. After the projection, the differential equation (4) becomes

$$\begin{aligned}
\frac{d}{dt}\begin{pmatrix} \mathbf{m} \\ 1 \end{pmatrix} &= -\gamma_{\tau, r_{p,\tau}} \begin{pmatrix} \mathrm{m}_y(\mathrm{m}_x\mathrm{B}_y - \mathrm{m}_y\mathrm{B}_x) - (\mathrm{B}_x - \mathrm{m}_x) \\ (\mathrm{m}_y - \mathrm{B}_y) - \mathrm{m}_x(\mathrm{m}_x\mathrm{B}_y - \mathrm{m}_y\mathrm{B}_x) \\ \mathrm{m}_x(\mathrm{B}_x - \mathrm{m}_x) - \mathrm{m}_y(\mathrm{m}_y - \mathrm{B}_y) \end{pmatrix} \\
&= -\gamma_{\tau, r_{p,\tau}} \begin{pmatrix} \mathrm{m}_y\mathrm{m}_x\mathrm{B}_y - \mathrm{m}_y^2\mathrm{B}_x - \mathrm{B}_x + \mathrm{m}_x \\ \mathrm{m}_y - \mathrm{B}_y - \mathrm{m}_x^2\mathrm{B}_y + \mathrm{m}_x\mathrm{m}_y\mathrm{B}_x \\ \mathrm{m}_x\mathrm{B}_x - \mathrm{m}_x^2 - \mathrm{m}_y^2 + \mathrm{m}_y\mathrm{B}_y \end{pmatrix} \\
&\approx -\gamma_{\tau, r_{p,\tau}} \begin{pmatrix} \mathrm{m}_x - \mathrm{B}_x \\ \mathrm{m}_y - \mathrm{B}_y \\ 0 \end{pmatrix} \\
&= -\gamma_{\tau, r_{p,\tau}} \begin{pmatrix} \mathbf{m} - \mathbf{b} \\ 0 \end{pmatrix}
\end{aligned}$$

where the approximation follows from the fact that the x- and y-coordinates of the vectors $\mathbf{e_B}(t)$ and $\mathbf{e_m}(t)$ are close to zero. Therefore, we can approximate products of them by zero.

For $t \geq \tau + r_{p,\tau}$ we have $\gamma(t) = 0$ and the right-hand side of the differential equation in (4) is zero. The same holds true for the differential equation in (5) and the approximation is valid.

Appendix B

By using the age depth model in (7) we derive a new function defined over depth as follows

$$\begin{aligned}
\mathbf{m}_p(t) &= \mathbf{m}_p(\tau + r_{p,\tau}) \\
&= \mathrm{e}^{-\Gamma_{\tau, r_{p,\tau}}(\tau + r_{p,\tau})} \left(\mathbf{b}(\tau) + \int_{\tau}^{\tau + r_{p,\tau}} \mathrm{e}^{\Gamma_{\tau, r_{p,\tau}}(t')} \gamma_{\tau, r_{p,\tau}}(t') \mathbf{b}(t') dt' \right) \\
&= \mathrm{e}^{-\int_{\tau}^{\tau + r_{p,\tau}} \gamma_{\tau, r_{p,\tau}}(\rho) d\rho} \left(\mathbf{b}(\tau) + \int_{\tau}^{\tau + r_{p,\tau}} \mathrm{e}^{\int_{\tau}^{t'} \gamma_{\tau, r_{p,\tau}}(\rho) d\rho} \gamma_{\tau, r_{p,\tau}}(t') \mathbf{b}(t') dt' \right) \\
&\overset{\varphi(z') := t'}{=} \mathrm{e}^{-\int_{\tau}^{\tau + r_{p,\tau}} \gamma_{\tau, r_{p,\tau}}(\rho) d\rho} \Bigg(\mathbf{b}(\tau) \\
&\qquad + \int_{\varphi^{-1}(\tau)}^{\varphi^{-1}(\tau + r_{p,\tau})} \mathrm{e}^{\int_{\tau}^{\varphi(z')} \gamma_{\tau, r_{p,\tau}}(\rho) d\rho} \gamma_{\tau, r_{p,\tau}}(\varphi(z')) \mathbf{b}(\varphi(z')) \varphi'(z') dz' \Bigg) \\
&\overset{\varphi(\zeta) := \rho}{=} \mathrm{e}^{-\int_{\varphi^{-1}(\tau)}^{\varphi^{-1}(\tau + r_{p,\tau})} \gamma_{\tau, r_{p,\tau}}(\varphi(\zeta)) \varphi'(\zeta) d\zeta} \Bigg(\mathbf{b}(\tau) \\
&\qquad + \int_{\varphi^{-1}(\tau)}^{\varphi^{-1}(\tau + r_{p,\tau})} \mathrm{e}^{\int_{\varphi^{-1}(\tau)}^{z'} \gamma_{\tau, r_{p,\tau}}(\varphi(\zeta)) \varphi'(\zeta) d\zeta} \gamma_{\tau, r_{p,\tau}}(\varphi(z')) \mathbf{b}(\varphi(z')) \varphi'(z') dz' \Bigg)
\end{aligned}$$

Now we define a new function $\tilde{\gamma}_{\varphi^{-1}(t)}(x) \coloneqq \gamma_t(\varphi(x))\varphi'(x)$ and get

$$
\begin{aligned}
\mathbf{m}_p(t) &= \mathrm{e}^{-\int_{\varphi^{-1}(\tau)}^{\varphi^{-1}(\tau+r_{p,\tau})} \tilde{\gamma}_{\varphi^{-1}(\tau+r_{p,\tau})}(\zeta)d\zeta} \Bigg(\mathbf{b}(\tau) \\
&\qquad + \int_{\varphi^{-1}(\tau)}^{\varphi^{-1}(\tau+r_{p,\tau})} \mathrm{e}^{\int_{\varphi^{-1}(\tau)}^{z'} \tilde{\gamma}_{\varphi^{-1}(\tau+r_{p,\tau})}(\zeta)d\zeta} \tilde{\gamma}_{\varphi^{-1}(\tau+r_{p,\tau})}(z')\mathbf{b}(\varphi(z'))dz'\Bigg) \\
&\overset{\zeta\coloneqq\varphi^{-1}(\tau)-\zeta}{=} \mathrm{e}^{\int_0^{\varphi^{-1}(\tau)-\varphi^{-1}(\tau+r_{p,\tau})} \tilde{\gamma}_{\varphi^{-1}(\tau+r_{p,\tau})}(\varphi^{-1}(\tau)-\zeta)d\zeta} \Bigg(\mathbf{b}(\tau) \\
&\qquad + \int_{\varphi^{-1}(\tau)}^{\varphi^{-1}(\tau+r_{p,\tau})} \mathrm{e}^{-\int_0^{\varphi^{-1}(\tau)-z'} \tilde{\gamma}_{\varphi^{-1}(\tau+r_{p,\tau})}(\varphi^{-1}(\tau)-\zeta)d\zeta} \tilde{\gamma}_{\varphi^{-1}(\tau+r_{p,\tau})}(z')\mathbf{b}(\varphi(z'))dz'\Bigg) \\
&\overset{(7)}{=} \mathrm{e}^{\int_0^{r_p} \tilde{\gamma}_{\varphi^{-1}(\tau+r_{p,\tau})}(\varphi^{-1}(\tau)-\zeta)d\zeta} \Bigg(\mathbf{b}(\tau) \\
&\qquad + \int_{\varphi^{-1}(\tau)}^{\varphi^{-1}(\tau+r_{p,\tau})} \mathrm{e}^{-\int_0^{\varphi^{-1}(\tau)-z'} \tilde{\gamma}_{\varphi^{-1}(\tau+r_{p,\tau})}(\varphi^{-1}(\tau)-\zeta)d\zeta} \tilde{\gamma}_{\varphi^{-1}(\tau+r_{p,\tau})}(z')\mathbf{b}(\varphi(z'))dz'\Bigg) \\
&\overset{z'\coloneqq\varphi^{-1}(\tau)-z'}{=} \mathrm{e}^{\int_0^{r_P} \tilde{\gamma}_{\varphi^{-1}(\tau+r_{p,\tau})}(\varphi^{-1}(\tau)-\zeta)d\zeta} \Bigg(\mathbf{b}(\tau) \\
&\qquad - \int_0^{r_p} \mathrm{e}^{-\int_0^{z'} \tilde{\gamma}_{\varphi^{-1}(\tau+r_{p,\tau})}(\varphi^{-1}(\tau)-\zeta)d\zeta} \tilde{\gamma}_{\varphi^{-1}(\tau+r_{p,\tau})}(\varphi^{-1}(\tau)-z')\mathbf{b}(\varphi(\varphi^{-1}(\tau)-z'))dz'\Bigg) \\
&\overset{\tilde{\gamma}_b(a-x)=\tilde{\gamma}_{b-a}(-x)}{=} \mathrm{e}^{\int_0^{r_p} \tilde{\gamma}_{-r_p}(-\zeta)d\zeta} \left(\mathbf{b}(\tau) - \int_0^{r_p} \mathrm{e}^{-\int_0^{z'} \tilde{\gamma}_{-r_p}(-\zeta)d\zeta} \tilde{\gamma}_{-r_P}(-z')\mathbf{b}(\varphi(\varphi^{-1}(\tau)-z'))dz'\right) \\
&\overset{\hat{\gamma}_{r_p}(x)\coloneqq-\tilde{\gamma}_{-r_p}(-x)}{=} \mathrm{e}^{-\int_0^{r_p} \hat{\gamma}_{r_p}(\zeta)d\zeta} \left(\mathbf{b}(\tau) + \int_0^{r_p} \mathrm{e}^{\int_0^{z'} \hat{\gamma}_{r_p}(\zeta)d\zeta} \hat{\gamma}_{r_p}(z')\mathbf{b}(\varphi(\varphi^{-1}(\tau)-z'))dz'\right) \\
&= \mathrm{e}^{-\hat{\Gamma}_{r_p}(r_p)} \left(\mathbf{b}(\tau) + \int_0^{r_p} \mathrm{e}^{\hat{\Gamma}_{r_p}(z')}\hat{\gamma}_{r_p}(z')\mathbf{b}(\varphi(\varphi^{-1}(\tau)-z'))dz'\right) \\
&\overset{\tilde{\mathbf{b}}(x)\coloneqq\mathbf{b}(\varphi(x))}{=} \mathrm{e}^{-\hat{\Gamma}_{r_p}(r_p)} \left(\mathbf{b}(\tau) + \int_0^{r_p} \mathrm{e}^{\hat{\Gamma}_{r_p}(z')}\hat{\gamma}_{r_p}(z')\tilde{\mathbf{b}}(\varphi^{-1}(\tau)-z')dz'\right)
\end{aligned}
$$

By setting $\varphi(z) = \tau$ we get a function $\tilde{\mathbf{m}}_p \colon \mathbb{R} \to \mathbb{R}^2$ with

$$
\begin{aligned}
\tilde{\mathbf{m}}_p(z) &= \mathbf{m}_p(\varphi(z)) \\
&= \mathrm{e}^{-\hat{\Gamma}_{r_p}(r_p)} \left(\mathbf{b}(\varphi(z)) + \int_0^{r_p} \mathrm{e}^{\hat{\Gamma}_{r_p}(z')}\hat{\gamma}_{r_p}(z')\tilde{\mathbf{b}}(z-z')dz'\right) \\
&= \mathrm{e}^{-\hat{\Gamma}_{r_p}(r_p)} \left(\tilde{\mathbf{b}}(z) + \int_0^{r_p} \mathrm{e}^{\hat{\Gamma}_{r_p}(z')}\hat{\gamma}_{r_p}(z')\tilde{\mathbf{b}}(z-z')dz'\right)
\end{aligned}
$$

Appendix C

In this section we present the derivations of the formulas used in the section 2.4.

$$
\begin{aligned}
\mathbf{\Sigma}_k^- &= \mathbf{F}\mathbf{\Sigma}_{k-1}\mathbf{F}^\top + \tilde{\mathbf{\Sigma}} \\
&= \begin{pmatrix} \mathrm{F} & \mathbf{0}_{1,n-1} \\ \mathbf{1}_{n-1,n-1} & \mathbf{0}_{n-1,1} \end{pmatrix} \begin{pmatrix} \mathbf{\Sigma}_{k-1}^{1:n-1,1:n-1} & \mathbf{\Sigma}_{k-1}^{1:n-1,n} \\ \mathbf{\Sigma}_{k-1}^{n,1:n-1} & \mathbf{\Sigma}_{k-1}^{n,n} \end{pmatrix} \begin{pmatrix} \mathrm{F}^\top & \mathbf{1}_{n-1,n-1} \\ \mathbf{0}_{n-1,1} & \mathbf{0}_{1,n-1} \end{pmatrix} + \tilde{\mathbf{\Sigma}} \\
&= \begin{pmatrix} \mathrm{F} & \mathbf{0}_{1,n-1} \\ \mathbf{1}_{n-1,n-1} & \mathbf{0}_{n-1,1} \end{pmatrix} \begin{pmatrix} \mathbf{\Sigma}_{k-1}^{1:n-1,1}\mathrm{F}^\top & \mathbf{\Sigma}_{k-1}^{1:n-1,1:n-1} \\ \mathbf{\Sigma}_{k-1}^{n,1}\mathrm{F}^\top & \mathbf{\Sigma}_{k-1}^{n,1:n-1} \end{pmatrix} + \begin{pmatrix} \tilde{\Sigma} & \mathbf{0}_{1,n-1} \\ \mathbf{0}_{n-1,1} & \mathbf{0}_{n-1,n-1} \end{pmatrix} \\
&= \begin{pmatrix} \mathrm{F}\mathbf{\Sigma}_{k-1}^{1,1}\mathrm{F}^\top + \tilde{\Sigma} & \mathrm{F}\mathbf{\Sigma}_{k-1}^{1,1:n-1} \\ \mathbf{\Sigma}_{k-1}^{1:n-1,1}\mathrm{F}^\top & \mathbf{\Sigma}_{k-1}^{1:n-1,1:n-1} \end{pmatrix}
\end{aligned}
$$

The backward recursion equations are derived as follows

$$
\begin{aligned}
\boldsymbol{\Sigma}_{k+1}^{-} &= \mathbf{F}\boldsymbol{\Sigma}_k\mathbf{F}^\top + \tilde{\boldsymbol{\Sigma}} = \begin{pmatrix} \mathrm{F}\boldsymbol{\Sigma}_k^{1,1}\mathrm{F}^\top + \tilde{\Sigma} & \mathrm{F}\boldsymbol{\Sigma}_k^{1,1:n-1} \\ \boldsymbol{\Sigma}_k^{1:n-1,1}\mathrm{F}^\top & \boldsymbol{\Sigma}_k^{1:n-1,1:n-1} \end{pmatrix} \\
\mathbf{G}_k &= \boldsymbol{\Sigma}_k\mathbf{F}^\top(\boldsymbol{\Sigma}_{k+1}^{-})^{-1} \\
&= \boldsymbol{\Sigma}_k \begin{pmatrix} \mathrm{F}^\top & \mathbf{1}_{n-1,n-1} \\ \mathbf{0}_{n-1,1} & \mathbf{0}_{1,n-1} \end{pmatrix} \begin{pmatrix} \tilde{\Sigma}^{-1} & \begin{pmatrix} -\tilde{\Sigma}^{-1}\mathrm{F} & \mathbf{0}_{1,n-2} \end{pmatrix} \\ \begin{pmatrix} -\mathrm{F}^\top\tilde{\Sigma}^{-1} \\ \mathbf{0}_{n-2,1} \end{pmatrix} & \begin{pmatrix} \mathbf{D}^{-1} + \mathrm{F}^\top\tilde{\Sigma}^{-1}\mathrm{F} & \mathbf{0}_{1,n-2} \\ \mathbf{0}_{n-2,1} & \mathbf{0}_{n-2,n-2} \end{pmatrix} \end{pmatrix} \\
&= \begin{pmatrix} \mathbf{0}_{n-1,1} & \mathbf{1}_{n-1,n-1} \\ \mathbf{0}_{1,1} & \underbrace{\boldsymbol{\Sigma}_k^{n,1:n-1}\left(\boldsymbol{\Sigma}_k^{1:n-1,1:n-1}\right)^{-1}}_{=\mathbf{A}_k\in\mathbb{R}^{1\times n-1}} \end{pmatrix} \\
\boldsymbol{\mu}_k^s &= \boldsymbol{\mu}_k + \mathbf{G}_k\left(\boldsymbol{\mu}_{k+1}^s - \boldsymbol{\mu}_{k+1}^-\right) \\
&= \boldsymbol{\mu}_k + \begin{pmatrix} \mathbf{0}_{n-1,1} & \mathbf{1}_{n-1,n-1} \\ \mathbf{0}_{1,1} & \mathbf{A}_k \end{pmatrix} \begin{pmatrix} \mathbf{m}_{k+1}^{s,1} - \mathrm{F}\mathbf{m}_k^1 \\ \boldsymbol{\mu}_{k+1}^{s,2} - \boldsymbol{\mu}_k^1 \\ \vdots \\ \boldsymbol{\mu}_{k+1}^{s,n} - \boldsymbol{\mu}_k^{n-1} \end{pmatrix} \\
&= \boldsymbol{\mu}_k + \begin{pmatrix} \boldsymbol{\mu}_{k+1}^{s,2:n-1} - \boldsymbol{\mu}_k^{1:n-2} \\ \mathbf{A}_k\left(\boldsymbol{\mu}_{k+1}^{s,2:n} - \boldsymbol{\mu}_k^{1:n-1}\right) \end{pmatrix} \\
&= \begin{pmatrix} \boldsymbol{\mu}_{k+1}^{s,2:n-1} \\ \boldsymbol{\mu}_k^n + \mathbf{A}_k\left(\boldsymbol{\mu}_{k+1}^{s,2:n} - \boldsymbol{\mu}_k^{1:n-1}\right) \end{pmatrix} \\
\boldsymbol{\Sigma}_k^s &= \boldsymbol{\Sigma}_k + \mathbf{G}_k\left(\boldsymbol{\Sigma}_{k+1}^s - \boldsymbol{\Sigma}_{k+1}^-\right)\mathbf{G}_k^\top \\
&= \boldsymbol{\Sigma}_k + \begin{pmatrix} \mathbf{0}_{n-1,1} & \mathbf{1}_{n-1,n-1} \\ \mathbf{0}_{1,1} & \mathbf{A}_k \end{pmatrix} \begin{pmatrix} \boldsymbol{\Sigma}_{k+1}^{s,1,1} - \mathrm{F}\boldsymbol{\Sigma}_k^{1,1}\mathrm{F}^\top - \tilde{\Sigma} & \boldsymbol{\Sigma}_{k+1}^{s,1,2:n} - \mathrm{F}\boldsymbol{\Sigma}_k^{1,1:n-1} \\ \boldsymbol{\Sigma}_{k+1}^{s,2:n,1} - \boldsymbol{\Sigma}_k^{1:n-1,1}\mathrm{F}^\top & \boldsymbol{\Sigma}_{k+1}^{s,2:n,2:n} - \boldsymbol{\Sigma}_k^{1:n-1,1:n-1} \end{pmatrix} \mathbf{G}_k^\top \\
&= \boldsymbol{\Sigma}_k + \begin{pmatrix} \boldsymbol{\Sigma}_{k+1}^{s,2:n,1} - \boldsymbol{\Sigma}_k^{1:n-1,1}\mathrm{F}^\top & \boldsymbol{\Sigma}_{k+1}^{s,2:n,2:n} - \boldsymbol{\Sigma}_k^{1:n-1,1:n-1} \\ \mathbf{A}_k\left(\boldsymbol{\Sigma}_{k+1}^{s,2:n,1} - \boldsymbol{\Sigma}_k^{1:n-1,1}\mathrm{F}^\top\right) & \mathbf{A}_k\left(\boldsymbol{\Sigma}_{k+1}^{s,2:n,2:n} - \boldsymbol{\Sigma}_k^{1:n-1,1:n-1}\right) \end{pmatrix} \begin{pmatrix} \mathbf{0}_{1,n-1} & \mathbf{0}_{1,1} \\ \mathbf{1}_{n-1,n-1} & \mathbf{A}_k^\top \end{pmatrix} \\
&= \boldsymbol{\Sigma}_k + \begin{pmatrix} \boldsymbol{\Sigma}_{k+1}^{s,2:n,2:n} - \boldsymbol{\Sigma}_k^{1:n-1,1:n-1} & \left(\boldsymbol{\Sigma}_{k+1}^{s,2:n,2:n} - \boldsymbol{\Sigma}_k^{1:n-1,1:n-1}\right)\mathbf{A}_k^\top \\ \mathbf{A}_k\left(\boldsymbol{\Sigma}_{k+1}^{s,2:n,2:n} - \boldsymbol{\Sigma}_k^{1:n-1,1:n-1}\right) & \mathbf{A}_k\left(\boldsymbol{\Sigma}_{k+1}^{s,2:n,2:n} - \boldsymbol{\Sigma}_k^{1:n-1,1:n-1}\right)\mathbf{A}_k^\top \end{pmatrix} \\
&= \begin{pmatrix} \boldsymbol{\Sigma}_{k+1}^{s,2:n,2:n} & \boldsymbol{\Sigma}_k^{1:n-1,n} + \left(\boldsymbol{\Sigma}_{k+1}^{s,2:n,2:n} - \boldsymbol{\Sigma}_k^{1:n-1,1:n-1}\right)\mathbf{A}_k^\top \\ \boldsymbol{\Sigma}_k^{n,1:n-1} + \mathbf{A}_k\left(\boldsymbol{\Sigma}_{k+1}^{s,2:n,2:n} - \boldsymbol{\Sigma}_k^{1:n-1,1:n-1}\right) & \boldsymbol{\Sigma}_k^{n,n} + \mathbf{A}_k\left(\boldsymbol{\Sigma}_{k+1}^{s,2:n,2:n} - \boldsymbol{\Sigma}_k^{1:n-1,1:n-1}\right)\mathbf{A}_k^\top \end{pmatrix} \\
&= \begin{pmatrix} \boldsymbol{\Sigma}_{k+1}^{s,2:n,2:n} & \boldsymbol{\Sigma}_k^{1:n-1,n} + \boldsymbol{\Sigma}_{k+1}^{s,2:n,2:n}\mathbf{A}_k^\top - \boldsymbol{\Sigma}_k^{1:n-1,n} \\ \boldsymbol{\Sigma}_k^{n,1:n-1} + \mathbf{A}_k\boldsymbol{\Sigma}_{k+1}^{s,2:n,2:n} - \boldsymbol{\Sigma}_k^{n,1:n-1} & \boldsymbol{\Sigma}_k^{n,n} + \mathbf{A}_k\left(\boldsymbol{\Sigma}_{k+1}^{s,2:n,2:n} - \boldsymbol{\Sigma}_k^{1:n-1,1:n-1}\right)\mathbf{A}_k^\top \end{pmatrix} \\
&= \begin{pmatrix} \boldsymbol{\Sigma}_{k+1}^{s,2:n,2:n} & \boldsymbol{\Sigma}_{k+1}^{s,2:n,2:n}\mathbf{A}_k^\top \\ \mathbf{A}_k\boldsymbol{\Sigma}_{k+1}^{s,2:n,2:n} & \boldsymbol{\Sigma}_k^{n,n} + \mathbf{A}_k\left(\boldsymbol{\Sigma}_{k+1}^{s,2:n,2:n} - \boldsymbol{\Sigma}_k^{1:n-1,1:n-1}\right)\mathbf{A}_k^\top \end{pmatrix}
\end{aligned}
$$

Where the inverse of the matrix $\boldsymbol{\Sigma}_{k+1}^{-}$ is derived as follows. We define

$$
\boldsymbol{\Sigma}_{k+1}^{-} = \begin{pmatrix} \mathrm{F}\boldsymbol{\Sigma}_{k-1}^{1,1}\mathrm{F}^\top + \tilde{\Sigma} & \mathrm{F}\boldsymbol{\Sigma}_{k-1}^{1,1:n-1} \\ \boldsymbol{\Sigma}_{k-1}^{1:n-1,1}\mathrm{F}^\top & \boldsymbol{\Sigma}_{k-1}^{1:n-1,1:n-1} \end{pmatrix} = \begin{pmatrix} \mathbf{A} & \mathbf{B} \\ \mathbf{C} & \mathbf{D} \end{pmatrix}
$$

The inverse of $\boldsymbol{\Sigma}_{k+1}^{-}$ is then given by

$$
\begin{aligned}
\left(\boldsymbol{\Sigma}_{k+1}^{-}\right)^{-1} &= \begin{pmatrix} \left(\mathbf{A}-\mathbf{B}\mathbf{D}^{-1}\mathbf{C}\right)^{-1} & -\left(\mathbf{A}-\mathbf{B}\mathbf{D}^{-1}\mathbf{C}\right)^{-1}\mathbf{B}\mathbf{D}^{-1} \\ -\mathbf{D}^{-1}\mathbf{C}\left(\mathbf{A}-\mathbf{B}\mathbf{D}^{-1}\mathbf{C}\right)^{-1} & \mathbf{D}^{-1}+\mathbf{D}^{-1}\mathbf{C}\left(\mathbf{A}-\mathbf{B}\mathbf{D}^{-1}\mathbf{C}\right)^{-1}\mathbf{B}\mathbf{D}^{-1} \end{pmatrix} \\
&\overset{(\star)}{=} \begin{pmatrix} \tilde{\Sigma}^{-1} & -\tilde{\Sigma}^{-1}\mathbf{B}\mathbf{D}^{-1} \\ -\mathbf{D}^{-1}\mathbf{C}\tilde{\Sigma}^{-1} & \mathbf{D}^{-1}+\mathbf{D}^{-1}\mathbf{C}\tilde{\Sigma}^{-1}\mathbf{B}\mathbf{D}^{-1} \end{pmatrix} \\
&\overset{(\star\star)}{=} \begin{pmatrix} \tilde{\Sigma}^{-1} & -\tilde{\Sigma}^{-1}\begin{pmatrix}\mathrm{F} & \mathbf{0}_{1,n-2}\end{pmatrix} \\ -\begin{pmatrix}\mathrm{F}^{\top} \\ \mathbf{0}_{n-2,1}\end{pmatrix}\tilde{\Sigma}^{-1} & \mathbf{D}^{-1}+\begin{pmatrix}\mathrm{F}^{\top} \\ \mathbf{0}_{n-2,1}\end{pmatrix}\tilde{\Sigma}^{-1}\begin{pmatrix}\mathrm{F} & \mathbf{0}_{1,n-2}\end{pmatrix} \end{pmatrix} \\
&= \begin{pmatrix} \tilde{\Sigma}^{-1} & \begin{pmatrix}-\tilde{\Sigma}^{-1}\mathrm{F} & \mathbf{0}_{1,n-2}\end{pmatrix} \\ \begin{pmatrix}-\mathrm{F}^{\top}\tilde{\Sigma}^{-1} \\ \mathbf{0}_{n-2,1}\end{pmatrix} & \begin{pmatrix}\mathbf{D}^{-1}+\mathrm{F}^{\top}\tilde{\Sigma}^{-1}\mathrm{F} & \mathbf{0}_{1,n-2} \\ \mathbf{0}_{n-2,1} & \mathbf{0}_{n-2,n-2}\end{pmatrix} \end{pmatrix}
\end{aligned}
$$

where $(\star)$ follows since

$$
\begin{aligned}
\left(\mathbf{A}-\mathbf{B}\mathbf{D}^{-1}\mathbf{C}\right)^{-1} &= \left(\mathrm{F}\boldsymbol{\Sigma}_k^{1,1}\mathrm{F}^{\top}+\tilde{\Sigma}-\mathrm{F}\boldsymbol{\Sigma}_k^{1,1:n-1}\left(\boldsymbol{\Sigma}_k^{1:n-1,1:n-1}\right)^{-1}\boldsymbol{\Sigma}_k^{1:n-1,1}\mathrm{F}^{\top}\right)^{-1} \\
&= \left(\mathrm{F}\boldsymbol{\Sigma}_k^{1,1}\mathrm{F}^{\top}+\tilde{\Sigma}-\mathrm{F}\boldsymbol{\Sigma}_k^{1,1}\mathrm{F}^{\top}\right)^{-1} \\
&= \tilde{\Sigma}^{-1}
\end{aligned}
$$

and $(\star\star)$ follows since

$$
\begin{aligned}
\mathbf{D}^{-1}\mathbf{C} &= \left(\boldsymbol{\Sigma}_k^{1:n-1,1:n-1}\right)^{-1}\boldsymbol{\Sigma}_k^{1:n-1,1}\mathrm{F}^{\top} = \begin{pmatrix}\mathrm{F}^{\top} \\ \mathbf{0}_{n-2,1}\end{pmatrix} \\
\mathbf{B}\mathbf{D}^{-1} &= \mathrm{F}\boldsymbol{\Sigma}_k^{1,1:n-1}\left(\boldsymbol{\Sigma}_k^{1:n-1,1:n-1}\right)^{-1} = \begin{pmatrix}\mathrm{F} & \mathbf{0}_{1,n-2}\end{pmatrix}
\end{aligned}
$$

Appendix D

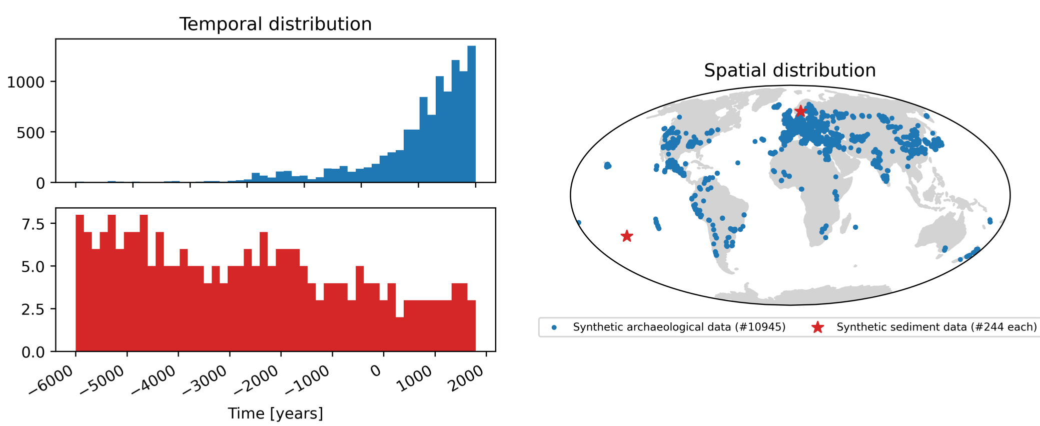

Figure D1. Spatial and temporal distribution of synthetic data

Open Research Section

All data used in this study as well as a python implementation of the method can be found in the GitLab repository (Bohsung & Schanner, 2023). On our website (https://sec23.git-pages.gfz-potsdam.de/korte/pdrm/) jupyter notebooks have been published that can be

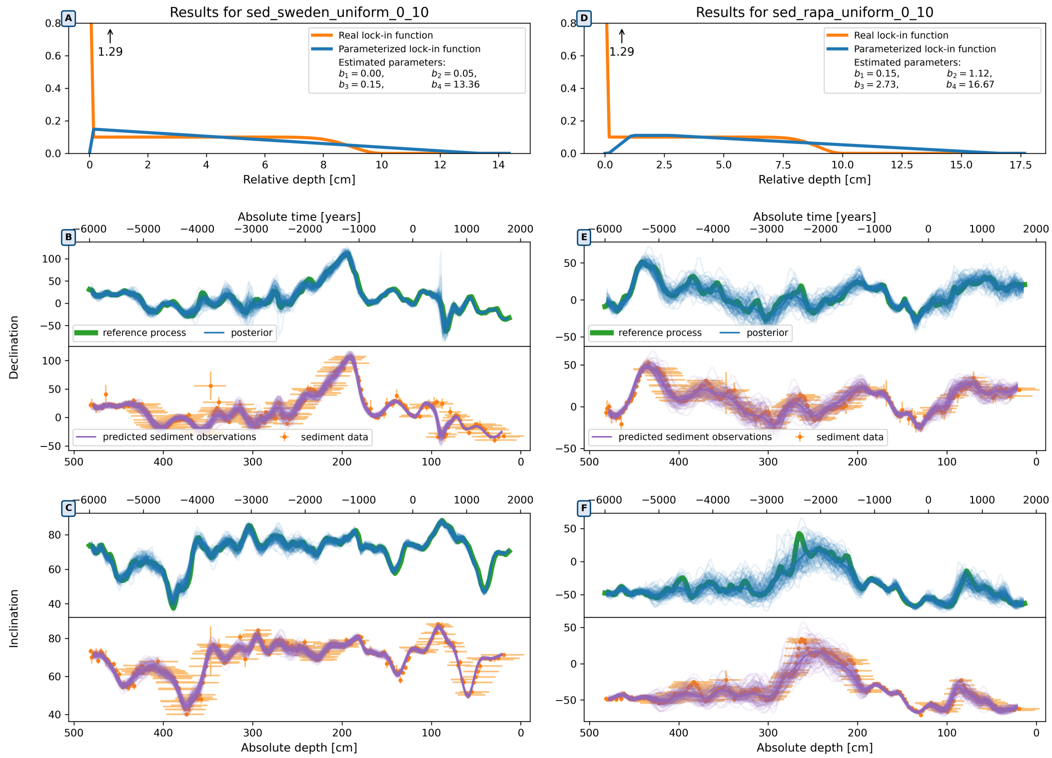

Figure D2. Results of modeling the pDRM for sed_sweden (left) and sed_rapa (right). Synthetic data are created from a reference process (green, (**B**) and (**E**) declination, (**C**) and (**F**) inclination) and distorted with the lock-in function (orange function in **A** and **D**) to form an input data series with uncertainties (orange points). Application of our lock-in model gives the posterior mean and 100 samples (blue in **B**, **C**, **E**, **F**) and estimated lock-in functions (blue in **A**, **B**). The mean and 100 samples of the posterior curves modified by the estimated lock-in function are also shown (purple in **B**, **C**, **E**, **F**).

used to generate more synthetic data or investigate cases which where not discussed in this paper. The raw data (KLK and GYL) for the two lakes in Sweden can be found on GEOMAGIA (Brown et al., 2015).

Acknowledgments

This work was funded by the Deutsche Forschungsgemeinschaft (DFG, German Research Foundation), grant 388291411. L. Bohsung and M. Schanner performed theoretical and conceptual work, with support of M. Korte and M. Holschneider. The manuscript was assembled by L. Bohsung with support from all co-authors. Software development and data processing was conducted by M. Schanner and L. Bohsung. The work and findings where supervised by M. Korte and M. Holschneider.

The authors wish to thank A. Nilsson and N. Nowaczyk for constructive and helpful discussions and comments that improved the quality of this study. We also thank A. Nilsson for sharing preprocessed sediment data from two lakes in Sweden.

References

Arneitz, P., Egli, R., Leonhardt, R., & Fabian, K. (2019). A bayesian iterative geo-

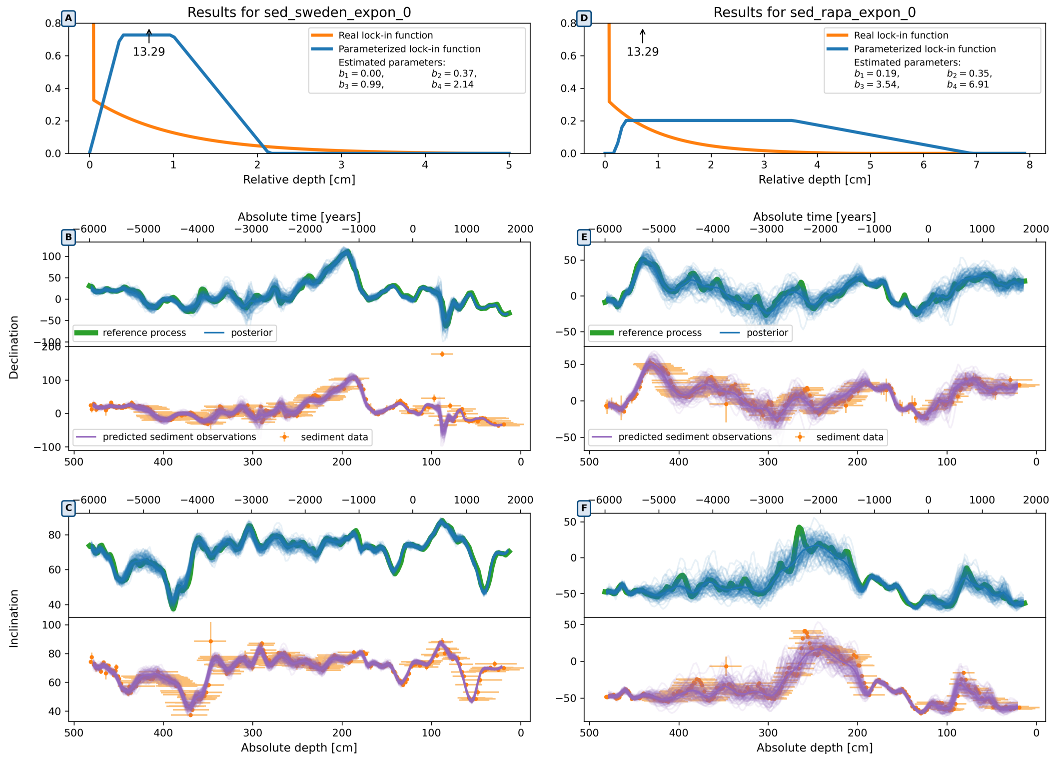

Figure D3. Results of modeling the pDRM for sed_sweden (left) and sed_rapa (right). Synthetic data are created from a reference process (green, (**B**) and (**E**) declination, (**C**) and (**F**) inclination) and distorted with the lock-in function (orange function in **A** and **D**) to form an input data series with uncertainties (orange points). Application of our lock-in model gives the posterior mean and 100 samples (blue in **B**, **C**, **E**, **F**) and estimated lock-in functions (blue in **A**, **B**). The mean and 100 samples of the posterior curves modified by the estimated lock-in function are also shown (purple in **B**, **C**, **E**, **F**).

magnetic model with universal data input: Self-consistent spherical harmonic evolution for the geomagnetic field over the last 4000 years. *Physics of the Earth and Planetary Interiors*, *290*, 57–75. doi: 10.1016/j.pepi.2019.03.008

Baerenzung, J., Holschneider, M., Wicht, J., Lesur, V., & Sanchez, S. (2020). The kalmag model as a candidate for igrf-13. *Earth, Planets and Space*, *72*, 1–13. doi: 10.1186/s40623-020-01295-y

Bleil, U., & Von Dobeneck, T. (1999). Geomagnetic events and relative paleointensity records—clues to high-resolution paleomagnetic chronostratigraphies of late quaternary marine sediments? *Use of Proxies in Paleoceanography: examples from the South Atlantic*, 635–654. doi: 10.1007/978-3-642-58646-0_26

Bohsung, L., & Schanner, M. (2023). *Modeling of the pdrm process.* `https://git.gfz-potsdam.de/sec23/korte/pdrm`. GitLab.

Brown, M. C., Donadini, F., Nilsson, A., Panovska, S., Frank, U., Korhonen, K., ... Constable, C. G. (2015). Geomagia50. v3: 2. a new paleomagnetic database for lake and marine sediments. *Earth, Planets and Space*, *67*, 1–19. doi: 10.1186/s40623-015-0233-z

Constable, C., Korte, M., & Panovska, S. (2016). Persistent high paleosecular variation activity in southern hemisphere for at least 10 000 years. *Earth and Planetary Science Letters*, *453*, 78–86. doi: 10.1016/j.epsl.2016.08.015

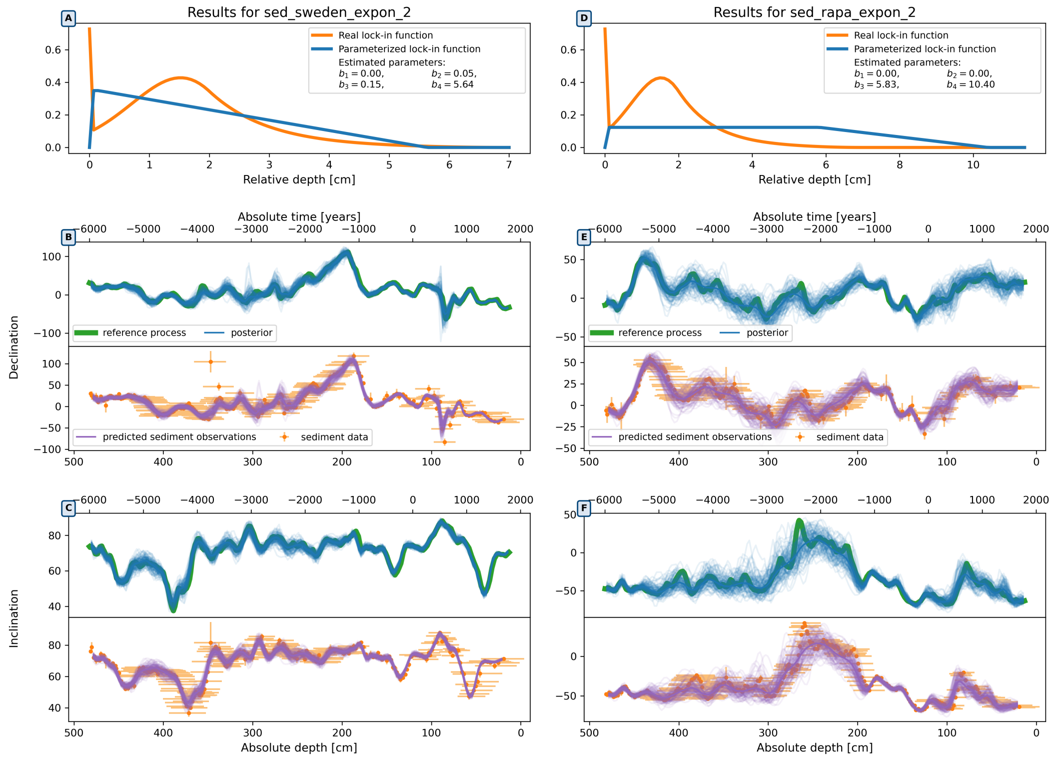

Figure D4. Results of modeling the pDRM for sed_sweden (left) and sed_rapa (right). Synthetic data are created from a reference process (green, (**B**) and (**E**) declination, (**C**) and (**F**) inclination) and distorted with the lock-in function (orange function in **A** and **D**) to form an input data series with uncertainties (orange points). Application of our lock-in model gives the posterior mean and 100 samples (blue in **B**, **C**, **E**, **F**) and estimated lock-in functions (blue in **A**, **B**). The mean and 100 samples of the posterior curves modified by the estimated lock-in function are also shown (purple in **B**, **C**, **E**, **F**).

Griffiths, D., King, R., Rees, A., & Wright, A. E. (1960). The remanent magnetism of some recent varved sediments. *Proceedings of the Royal Society of London. Series A. Mathematical and Physical Sciences*, *256*(1286), 359–383. doi: 10.1098/rspa.1960.0113

Hellio, G., & Gillet, N. (2018). Time-correlation-based regression of the geomagnetic field from archeological and sediment records. *Geophysical Journal International*, *214*(3), 1585–1607. doi: 10.1093/GJI/GGY214

Irving, E. (1957). Iii. the origin of the palaeomagnetism of the torridonian sandstones of north-west scotland. *Philosophical Transactions of the Royal Society of London. Series A, Mathematical and Physical Sciences*, *250*(974), 100–110. doi: 10.1098/rsta.1957.0014

Kalman, R. E. (1960, 03). A new approach to linear filtering and prediction problems. *Journal of Basic Engineering*, *82*(1), 35-45. doi: 10.1115/1.3662552

Kent, D. V., & Schneider, D. A. (1995). Correlation of paleointensity variation records in the brunhes/matuyama polarity transition interval. *Earth and Planetary Science Letters*, *129*(1-4), 135–144. doi: 10.1016/0012-821X(94)00236-R

King, R. (1955). The remanent magnetism of artificially deposited sediments. *Geophysical Supplements to the Monthly Notices of the Royal Astronomical Society*, *7*(3), 115–134. doi: 10.1111/j.1365-246X.1955.tb06558.x

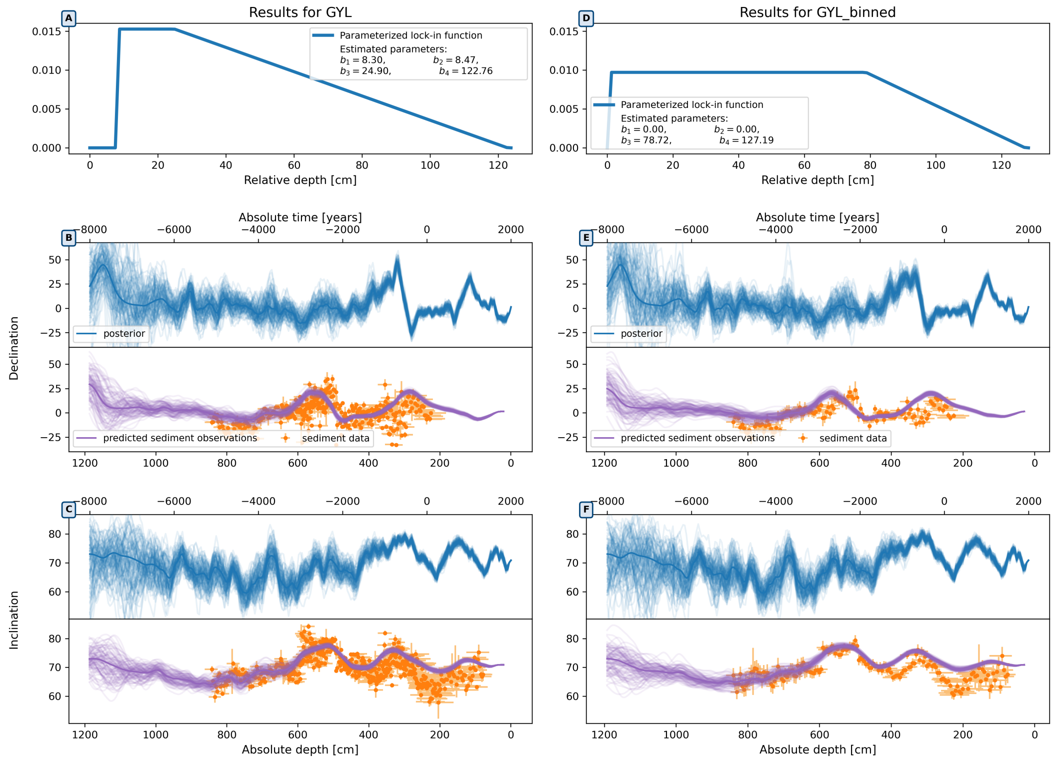

Figure D5. Results for GYL and GYL_binned.

Løvlie, R. (1976). The intensity pattern of post-depositional remanence acquired in some marine sediments deposited during a reversal of the external magnetic field. *Earth and Planetary Science Letters*, *30*(2), 209–214. doi: 10.1016/0012-821X(76)90247-8

McNish, A., & Johnson, E. (1938). Magnetization of unmetamorphosed varves and marine sediments. *Terrestrial Magnetism and Atmospheric Electricity*, *43*(4), 401–407. doi: 10.1029/TE043i004p00401

Mellström, A., Muscheler, R., Snowball, I., Ning, W., & Haltia, E. (2013). Radiocarbon wiggle-match dating of bulk sediments—how accurate can it be? *Radiocarbon*, *55*(3), 1173–1186. doi: 10.1017/S0033822200048086

Mellström, A., Nilsson, A., Stanton, T., Muscheler, R., Snowball, I., & Suttie, N. (2015). Post-depositional remanent magnetization lock-in depth in precisely dated varved sediments assessed by archaeomagnetic field models. *Earth and Planetary Science Letters*, *410*, 186–196. doi: 10.1016/j.epsl.2014.11.016

Meynadier, L., & Valet, J.-P. (1996). Post-depositional realignment of magnetic grains and asymmetrical saw-tooth patterns of magnetization intensity. *Earth and planetary science letters*, *140*(1-4), 123–132. doi: 10.1016/0012-821X(96)00018-0

Nilsson, A., & Suttie, N. (2021). Probabilistic approach to geomagnetic field modelling of data with age uncertainties and post-depositional magnetisations. *Physics of the Earth and Planetary Interiors*, *317*, 106737. doi: 10.1016/j.pepi.2021.106737

Nilsson, A., Suttie, N., & Hill, M. J. (2018). Short-term magnetic field variations from the post-depositional remanence of lake sediments. *Frontiers in Earth Science*, *6*, 39. doi: 10.3389/feart.2018.00039

Nilsson, A., Suttie, N., Stoner, J. S., & Muscheler, R. (2022). Recurrent ancient geomagnetic field anomalies shed light on future evolution of the south atlantic anomaly. *Proceedings of the National Academy of Sciences*, *119*(24), e2200749119. doi: 10.1073/pnas.2200749119

Rasmussen, C. E. (2004). Gaussian processes in machine learning. In O. Bousquet, U. von Luxburg, & G. Rätsch (Eds.), *Advanced lectures on machine learning: Ml summer schools 2003, canberra, australia, february 2 - 14, 2003, tübingen, germany, august 4 - 16, 2003, revised lectures* (pp. 63–71). Berlin, Heidelberg: Springer Berlin Heidelberg. doi: 10.1007/978-3-540-28650-9_4

Roberts, A. P., & Winklhofer, M. (2004). Why are geomagnetic excursions not always recorded in sediments? constraints from post-depositional remanent magnetization lock-in modelling. *Earth and Planetary Science Letters*, *227*(3-4), 345–359. doi: 10.1016/j.epsl.2004.07.040

Schanner, M., Korte, M., & Holschneider, M. (2022). Archkalmag14k: A kalman-filter based global geomagnetic model for the holocene. *Journal of Geophysical Research: Solid Earth*, *127*(2), e2021JB023166. doi: 10.1029/2021JB023166

Snowball, I., Mellström, A., Ahlstrand, E., Haltia, E., Nilsson, A., Ning, W., ... Brauer, A. (2013). An estimate of post-depositional remanent magnetization lock-in depth in organic rich varved lake sediments. *Global and planetary change*, *110*, 264–277. doi: 10.1016/j.gloplacha.2013.10.005

Stacey, F. (2012). *The physical principles of rock magnetism* (No. 5). Elsevier.

Stanton, T., Nilsson, A., Snowball, I., & Muscheler, R. (2011). Assessing the reliability of holocene relative palaeointensity estimates: a case study from swedish varved lake sediments. *Geophysical Journal International*, *187*(3), 1195–1214. doi: 10.1111/j.1365-246X.2011.05049.x

Stanton, T., Snowball, I., Zillén, L., & Wastegård, S. (2010). Validating a swedish varve chronology using radiocarbon, palaeomagnetic secular variation, lead pollution history and statistical correlation. *Quaternary Geochronology*, *5*(6), 611–624. doi: 10.1016/j.quageo.2010.03.004

Suganuma, Y., Okuno, J., Heslop, D., Roberts, A. P., Yamazaki, T., & Yokoyama, Y. (2011). Post-depositional remanent magnetization lock-in for marine sediments deduced from 10be and paleomagnetic records through the matuyama–brunhes boundary. *Earth and Planetary Science Letters*, *311*(1-2), 39–52. doi: 10.1016/j.epsl.2011.08.038

Verosub, K. L. (1977). Depositional and postdepositional processes in the magnetization of sediments. *Reviews of Geophysics*, *15*(2), 129–143. doi: 10.1029/RG015i002p00129

Figure 1.

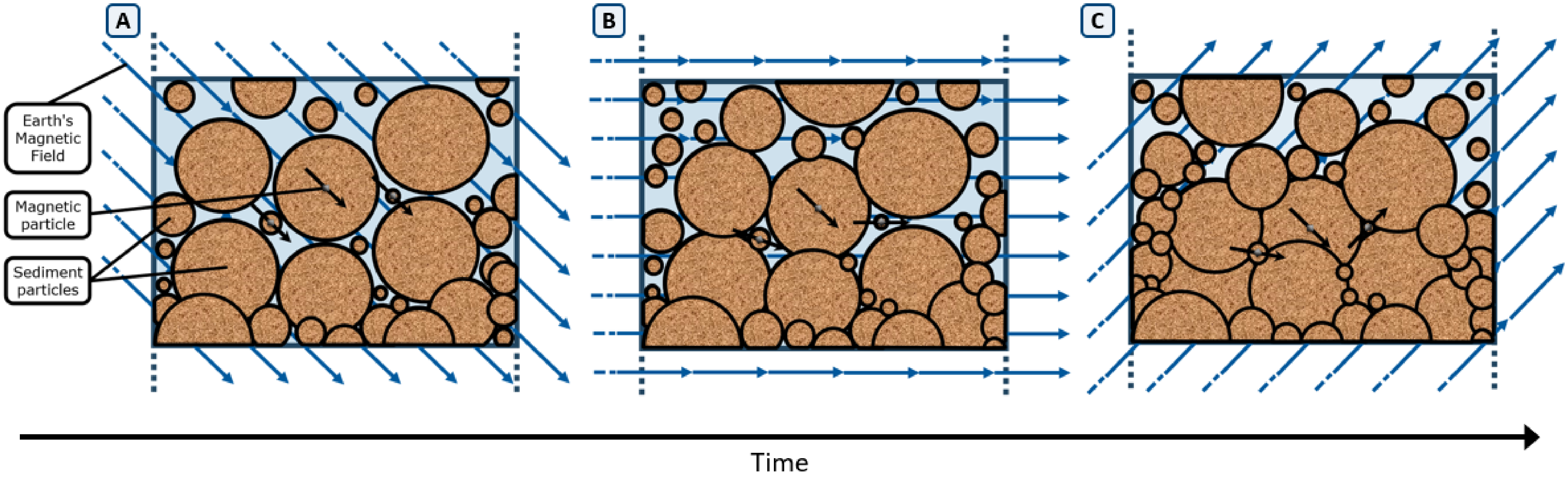

A
B
C
Earth's Magnetic Field
Magnetic particle
Sediment particles
Time

Figure 2.

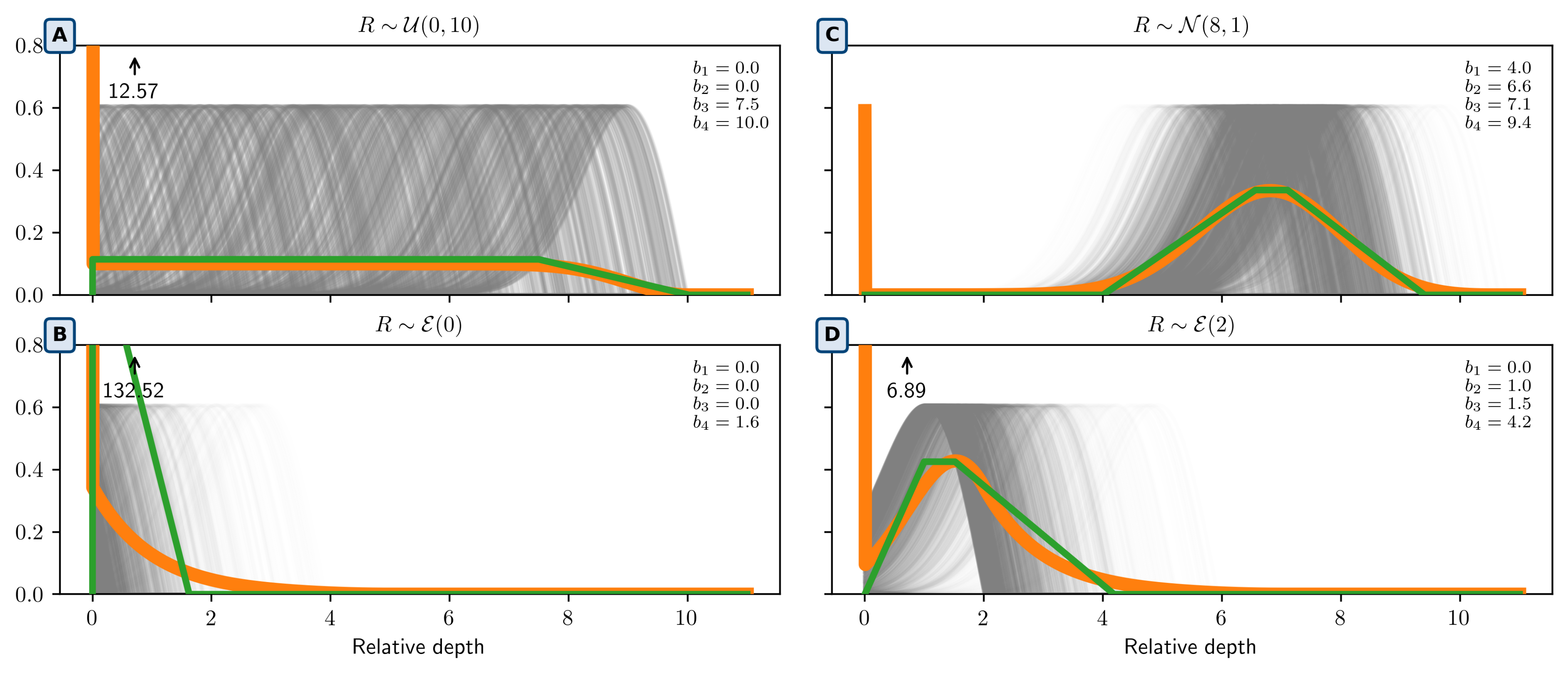
A
$R \sim \mathcal{U}(0,10)$
12.57
$b_1 = 0.0$
$b_2 = 0.0$
$b_3 = 7.5$
$b_4 = 10.0$
B
$R \sim \mathcal{E}(0)$
132.52
$b_1 = 0.0$
$b_2 = 0.0$
$b_3 = 0.0$
$b_4 = 1.6$
C
$R \sim \mathcal{N}(8,1)$
$b_1 = 4.0$
$b_2 = 6.6$
$b_3 = 7.1$
$b_4 = 9.4$
D
$R \sim \mathcal{E}(2)$
6.89
$b_1 = 0.0$
$b_2 = 1.0$
$b_3 = 1.5$
$b_4 = 4.2$
0.0
0.2
0.4
0.6
0.8
0
2
4
6
8
10
Relative depth

Figure 3.

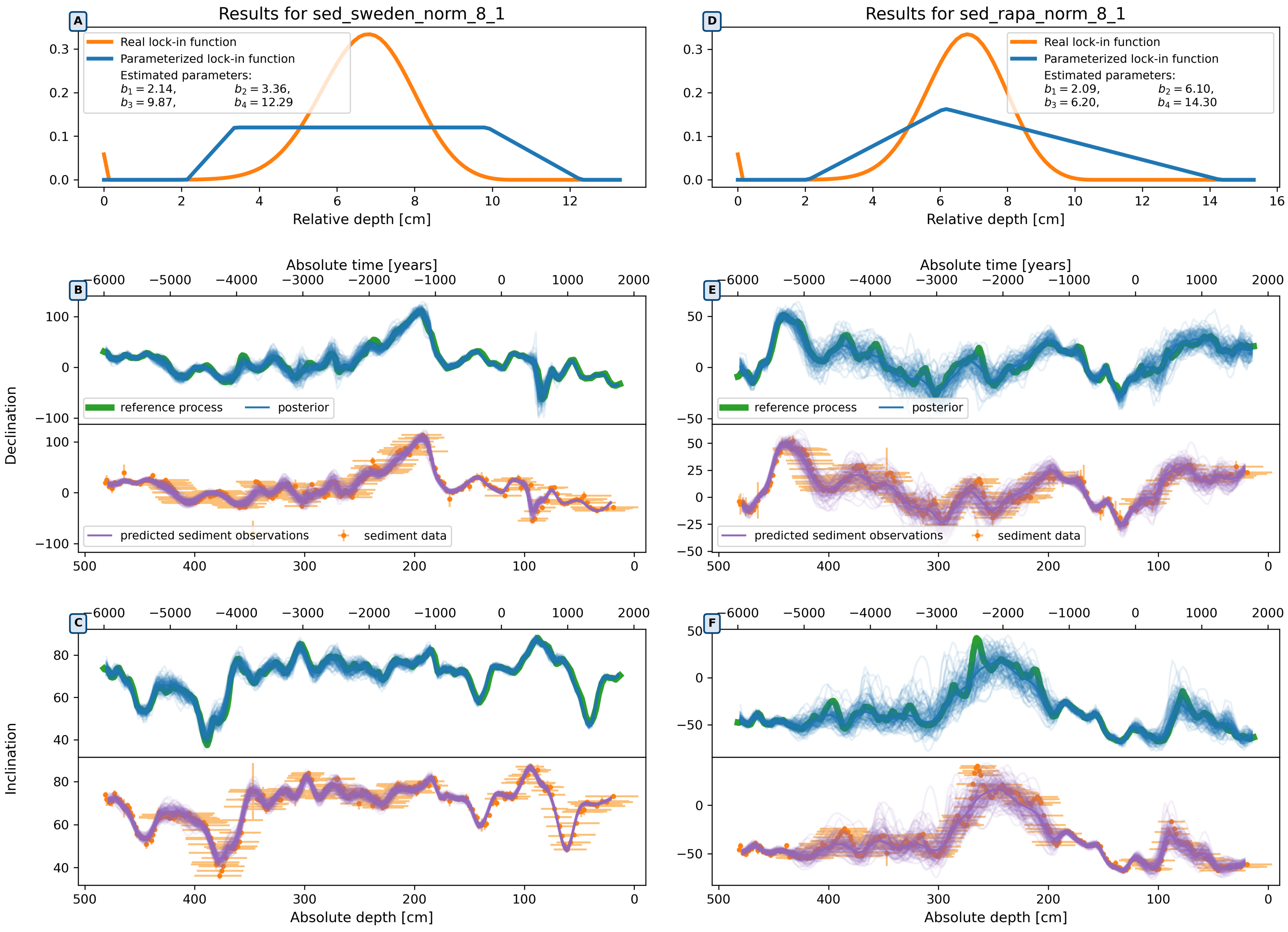

A
Results for sed_sweden_norm_8_1
Real lock-in function
Parameterized lock-in function
Estimated parameters:
$b_1 = 2.14$, $b_2 = 3.36$,
$b_3 = 9.87$, $b_4 = 12.29$
Relative depth [cm]
D
Results for sed_rapa_norm_8_1
Real lock-in function
Parameterized lock-in function
Estimated parameters:
$b_1 = 2.09$, $b_2 = 6.10$,
$b_3 = 6.20$, $b_4 = 14.30$
Relative depth [cm]
Absolute time [years]
B
E
Declination
reference process
posterior
predicted sediment observations
sediment data
Absolute time [years]
C
F
Inclination
Absolute depth [cm]

Figure 4.

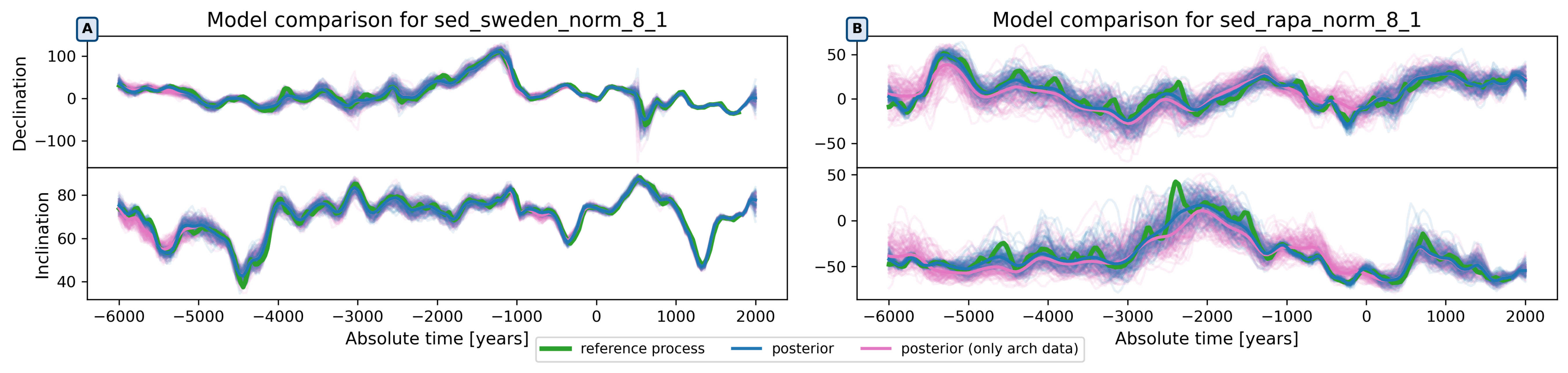

A
Model comparison for sed_sweden_norm_8_1
B
Model comparison for sed_rapa_norm_8_1
Declination
Inclination
Absolute time [years]
Absolute time [years]
reference process
posterior
posterior (only arch data)

Figure 5.

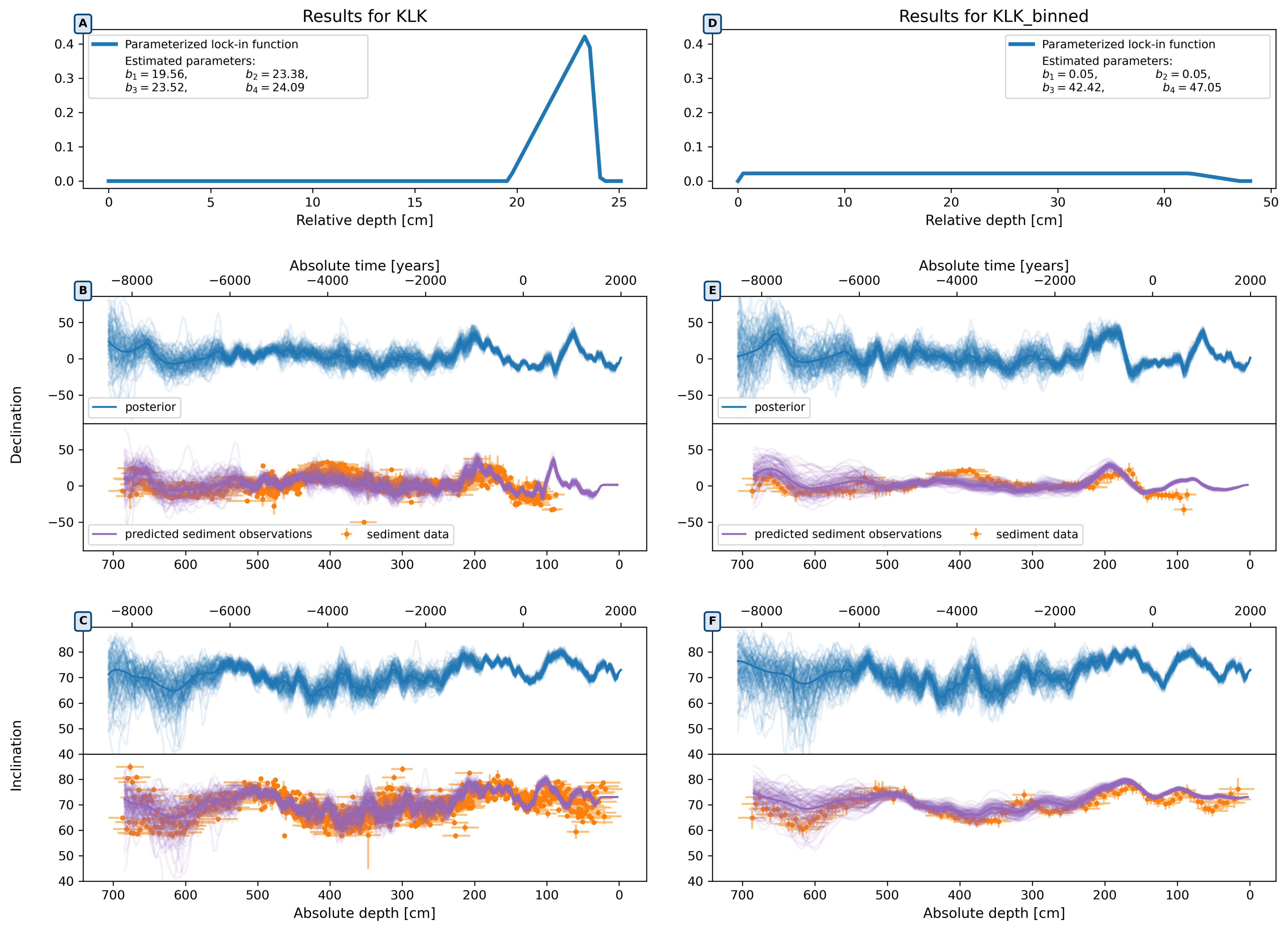

Results for KLK
Results for KLK_binned
A
B
C
D
E
F
Parameterized lock-in function
Estimated parameters:
$b_1 = 19.56$, $b_2 = 23.38$,
$b_3 = 23.52$, $b_4 = 24.09$
$b_1 = 0.05$, $b_2 = 0.05$,
$b_3 = 42.42$, $b_4 = 47.05$
Relative depth [cm]
Absolute time [years]
Declination
Inclination
posterior
predicted sediment observations
sediment data
Absolute depth [cm]

Figure D1.

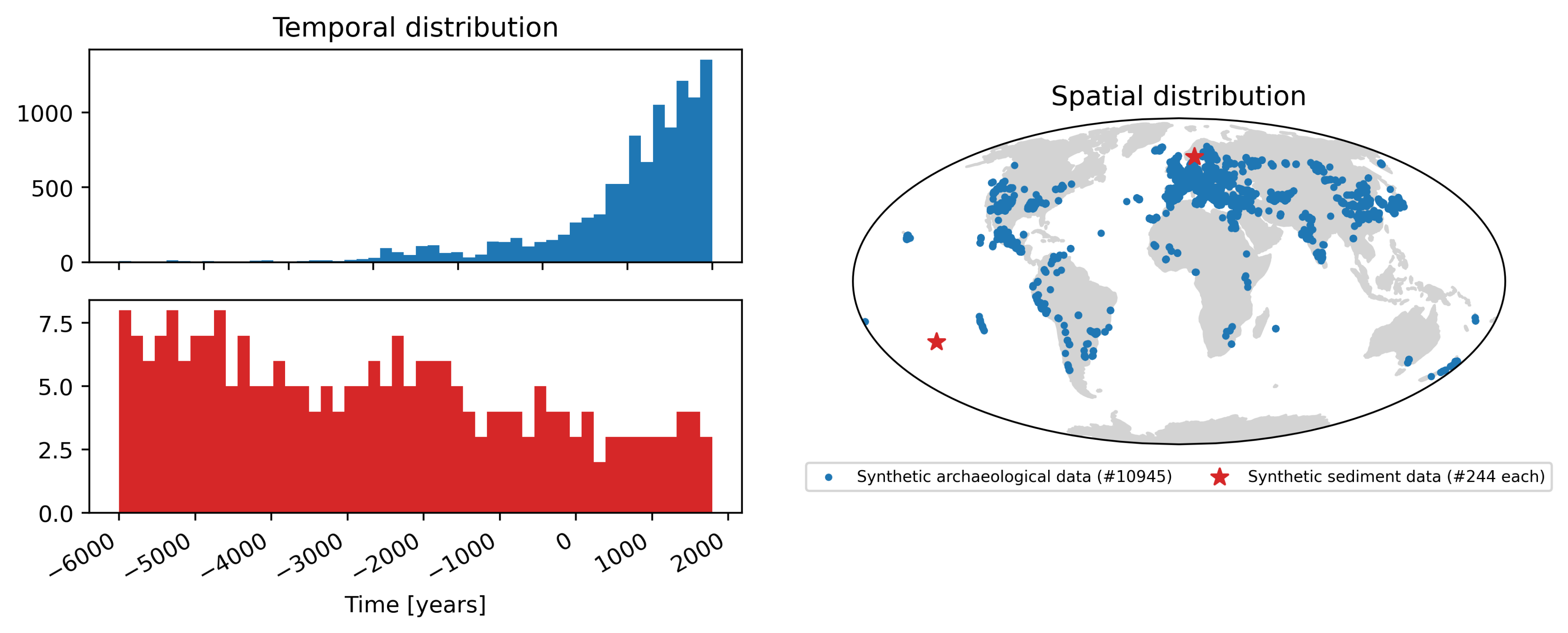
Temporal distribution
1000
500
0
7.5
5.0
2.5
0.0
−6000
−5000
−4000
−3000
−2000
−1000
0
1000
2000
Time [years]
Spatial distribution
Synthetic archaeological data (#10945)
Synthetic sediment data (#244 each)

Figure D2.

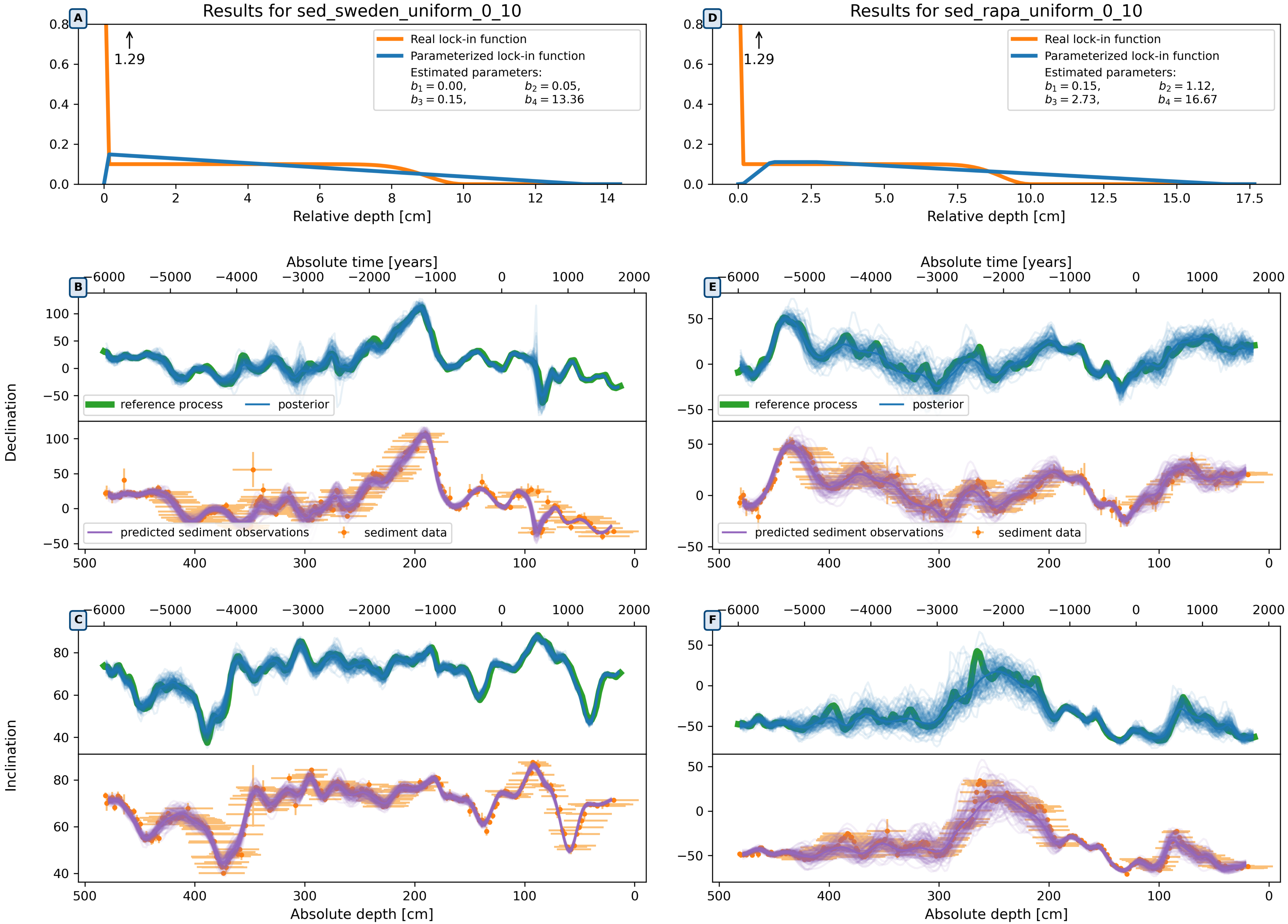

Results for sed_sweden_uniform_0_10
A
Real lock-in function
Parameterized lock-in function
Estimated parameters:
$b_1 = 0.00$, $b_2 = 0.05$,
$b_3 = 0.15$, $b_4 = 13.36$
1.29
Relative depth [cm]
Results for sed_rapa_uniform_0_10
D
Real lock-in function
Parameterized lock-in function
Estimated parameters:
$b_1 = 0.15$, $b_2 = 1.12$,
$b_3 = 2.73$, $b_4 = 16.67$
1.29
Relative depth [cm]
Absolute time [years]
B
E
reference process
posterior
predicted sediment observations
sediment data
Declination
C
F
Inclination
Absolute depth [cm]

Figure D3.

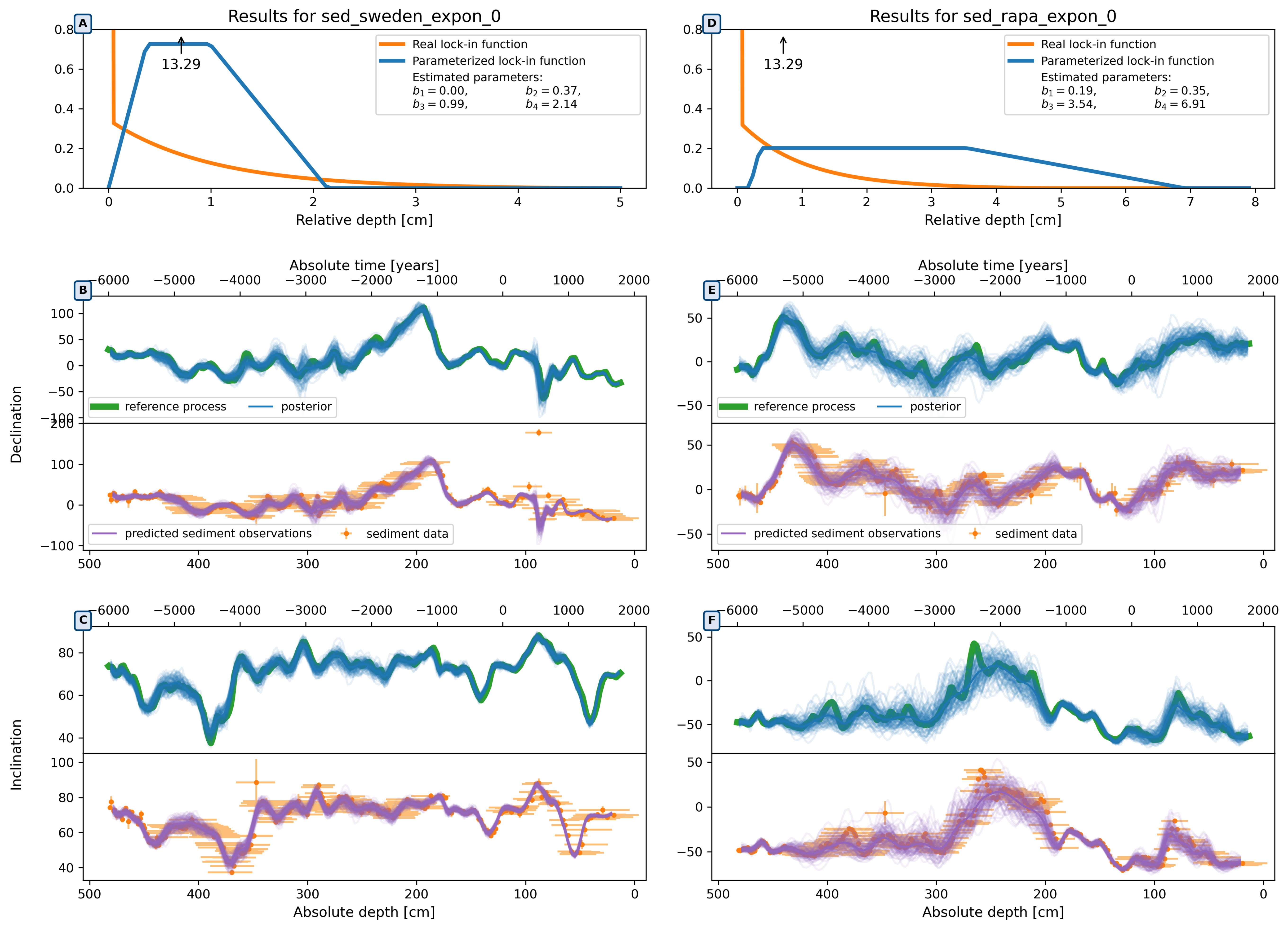

Results for sed_sweden_expon_0
A
Real lock-in function
Parameterized lock-in function
Estimated parameters:
$b_1 = 0.00$, $b_2 = 0.37$,
$b_3 = 0.99$, $b_4 = 2.14$
13.29
Relative depth [cm]
Results for sed_rapa_expon_0
D
Real lock-in function
Parameterized lock-in function
Estimated parameters:
$b_1 = 0.19$, $b_2 = 0.35$,
$b_3 = 3.54$, $b_4 = 6.91$
13.29
Relative depth [cm]
Absolute time [years]
B
E
reference process
posterior
predicted sediment observations
sediment data
Declination
C
F
Inclination
Absolute depth [cm]

Figure D4.

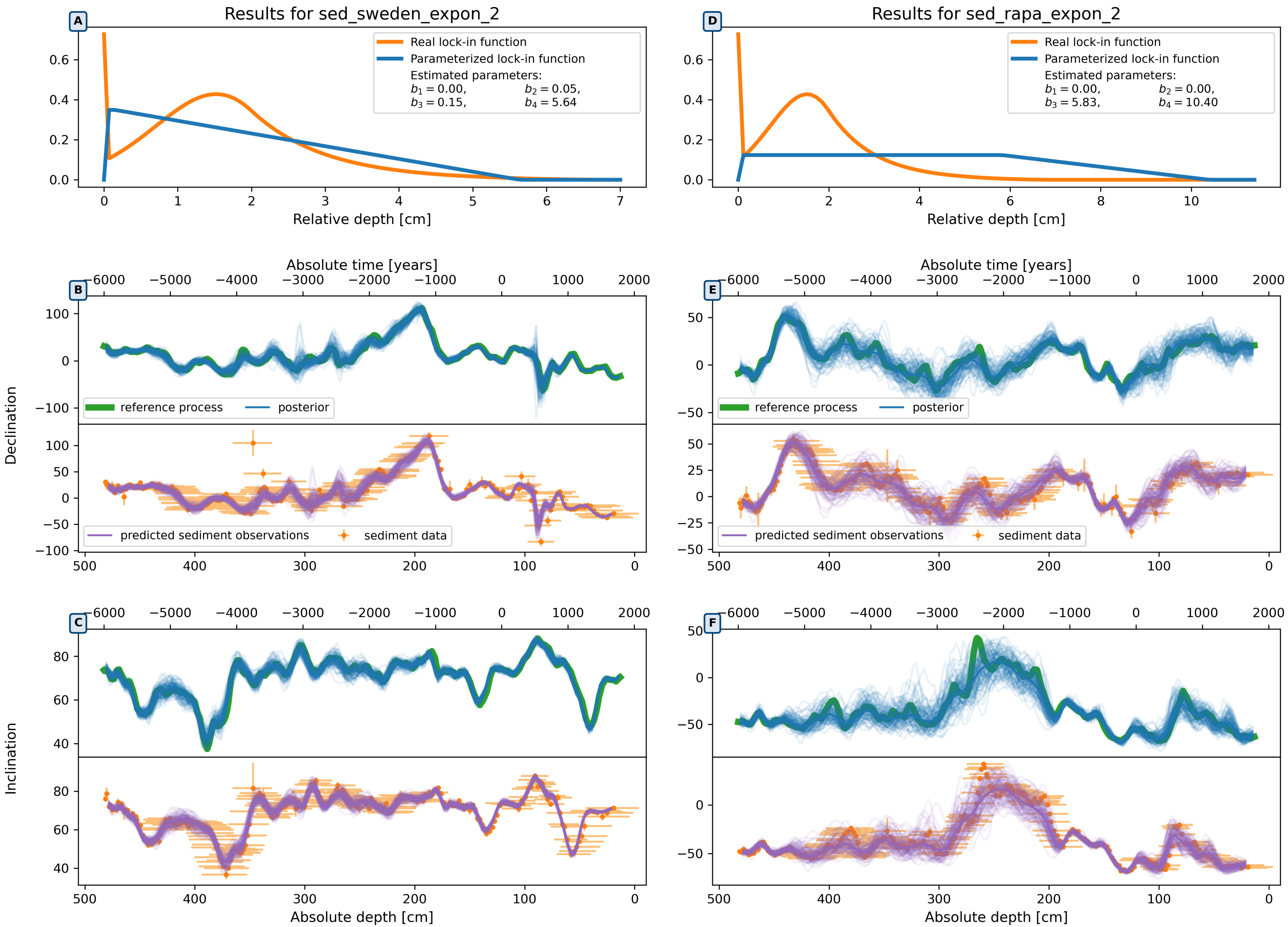
Results for sed_sweden_expon_2
Results for sed_rapa_expon_2
A
B
C
D
E
F
Real lock-in function
Parameterized lock-in function
Estimated parameters:
$b_1 = 0.00$, $b_2 = 0.05$,
$b_3 = 0.15$, $b_4 = 5.64$
$b_1 = 0.00$, $b_2 = 0.00$,
$b_3 = 5.83$, $b_4 = 10.40$
Relative depth [cm]
Absolute time [years]
Declination
Inclination
reference process
posterior
predicted sediment observations
sediment data
Absolute depth [cm]

Figure D5.

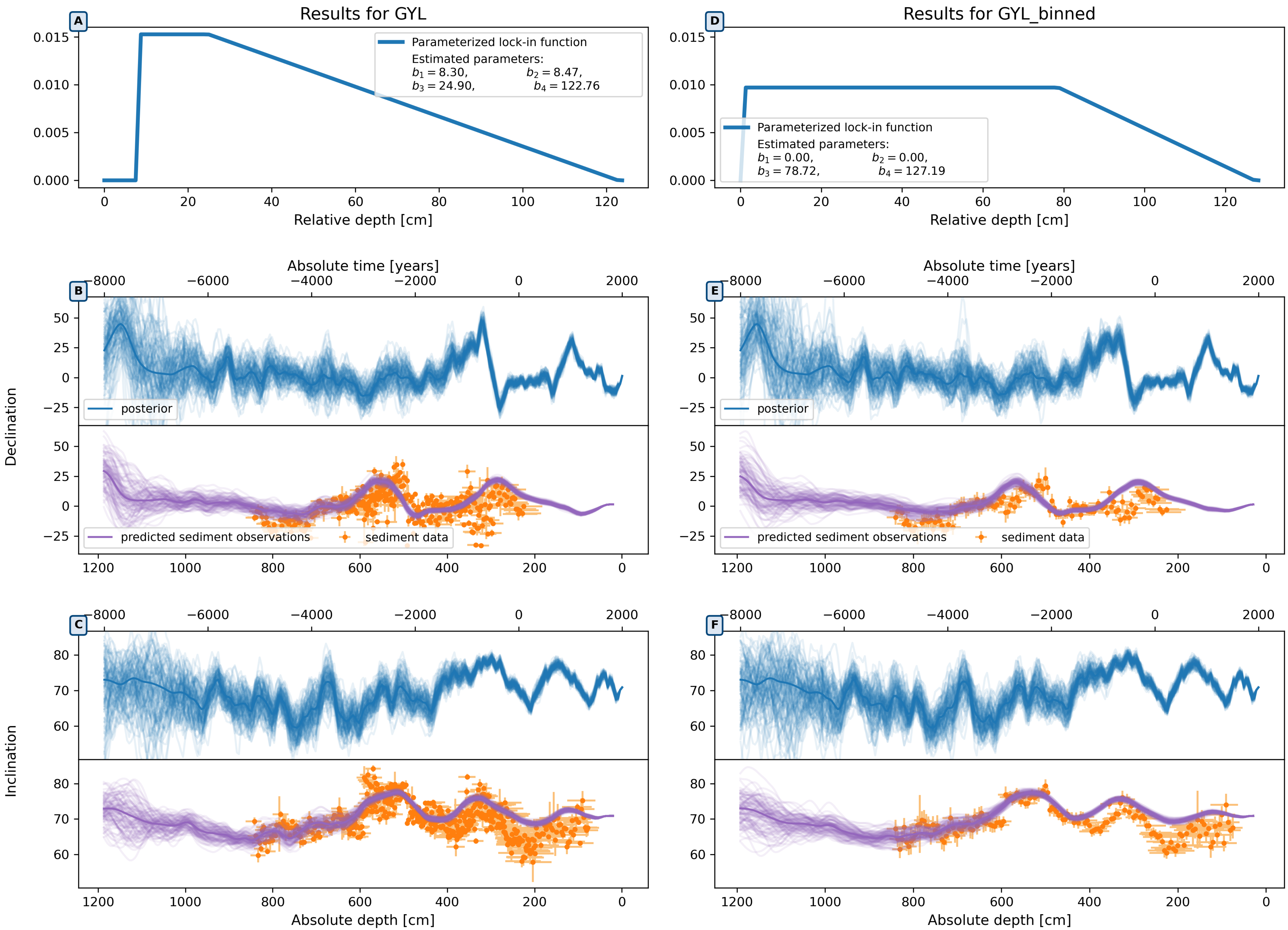

Results for GYL
Results for GYL_binned
A
B
C
D
E
F
Parameterized lock-in function
Estimated parameters:
$b_1 = 8.30$, $b_2 = 8.47$,
$b_3 = 24.90$, $b_4 = 122.76$
Estimated parameters:
$b_1 = 0.00$, $b_2 = 0.00$,
$b_3 = 78.72$, $b_4 = 127.19$
Relative depth [cm]
Absolute time [years]
Declination
Inclination
posterior
predicted sediment observations
sediment data
Absolute depth [cm]